UNIVERSITY OF CALIFORNIA

SANTA CRUZ

AN INCLUSIVE SEARCH FOR THE DECAY OF A BOOSTED HIGGS BOSON IN THE $H \to b\bar{b}$ CHANNEL WITH THE ATLAS DETECTOR

A dissertation submitted in partial satisfaction of the

requirements for the degree of

DOCTOR OF PHILOSOPHY

in

PARTICLE PHYSICS

by

Jacob Martin Pasner

October 2019

The Dissertation of Jacob Martin Pasner
is approved:

Professor Jason Nielsen, Chair

Professor Abraham Seiden

Professor Michael Hance

Dean Lori Kletzer
Vice Provost and Dean of Graduate Studies

Table of Contents

List of Figures

List of Tables

Abstract

An Inclusive Search for the decay of a Boosted Higgs boson in the $H \to b\bar{b}$ channel with the ATLAS detector

by

Jacob Martin Pasner

Abstract placeholder

Dedication

Dedication

Dedication

Acknowledgments

Chapter 1

Introduction

Every dissertation should have an introduction. You might not realize it, but the introduction should introduce the concepts, backgrouand, and goals of the dissertation.

Part I

Theoretical Motivations and the Standard Model

Chapter 2

The Standard Model and Beyond

The Standard Model (SM) of Particle Physics is humanities best ”guess” at the force laws that describe the observed behavior of all particles in our universe. Its formulation is a collection of Quantum Field Theories (QFT) that describe the following interactions of elementary matter in Nature: the electromagnetic force, the weak nuclear force and the strong nuclear force. Gravity is noticeably absent as currently there is no viable quantum theory for observed gravitational effects. The Glashow-Salam-Weinberg (GSW) theory of Quantum Electrodynamics (QED) describes the electromagnetic and weak forces, while Quantum Chromodyanmics (QCD) describes the strong force. These theories form the following symmetry group of the Standard Model.

$$\underbrace{\mathrm{SU_C}(3)}_{\mathrm{QCD}} \otimes \underbrace{\mathrm{SU_L}(2) \otimes \mathrm{U_Y}(1)}_{\mathrm{GSW}}. \tag{2.1}$$

The gauge principle states that the SM Lagrangian and its predictions must be invariant under local transformations using an operator from any of these constituent groups. Thus, any theory must only include transformations and terms that maintain the local invariance of the complete Lagrangian. In particular, this requirement was violated by any attempt to include an explicit mass term for the Gauge Bososns of QED and for all fermions. Around 1960 a possible solution to this lack of mass was proposed in the form of the spontaneous breaking of the ElectroWeak symmetry, now known as the Higgs mechanism. In the following sections I will go into more detail about the Lagrangian formalism of the Standard Model, QCD, QED and this recently verified Higgs Mechanism.

2.1 The Standard Model

At the turn of the 20th century our understaning of the constituent matter of the universe was limited to what we could see with microscopes and imply from the observations of light and elctricity, giving us evidence for both the photon and the electron. In the first half of the century we discovered the field of subatomic physics with Rutherfords 1911 gold foil scattering experiment, and Dirac successfully demonstrated the quantization of the electromagnetic field, the first step towards a fully Gauge Invariant Quantum Field Theory. In the second half we literally delved deeper, discovering that the nucleus contained structure and extended our theories to include the the complex mechanics of quarks and gluons. With the discovery of the Higgs in 2013 the Standard Model has become an irrefutable framework as can be seen in the high level of agreement betwee theory experiment in fig. 2.1.

The QCD and QED theories predict two classes of particles: fermions and bosons shown in fig. 2.2. These particles represent the quanta of the quantum fields of the Standard Model and the mediators of the fundamental forces of Nature.

2.1.1 Bosons

These spin-1 particles are known as the vector gauge bosons and are the force carriers of the SM. The most commonly known is the electromagnetic force's un-charged and massless photon (γ) which interacts with all charged particles and is often refered to as ”light”. The weak nuclear force is involved in nuclear interactions such as beta decays and is carried by 3 bosons all of which have mass and couple to all fermions; the $W^{\pm}$ bosons, which mediate the charged weak nuclear interaction and allow for flavor changing currents; and the Z boson which mediates the neutral weak nuclear interaction. Finally we have 8 massless gluons which mediate the strong nuclear force and only interact with fermions with a ”color” charge such as the quarks contained inside the nucleus. The only spin-0 boson, the Higgs Boson (h) is the key to generating mass terms in the SM Lagrangian for the massive Gauge Bosons and for fermions. This is done through the so called Higgs Mechanism and is discussed in more detail in section 2.4.

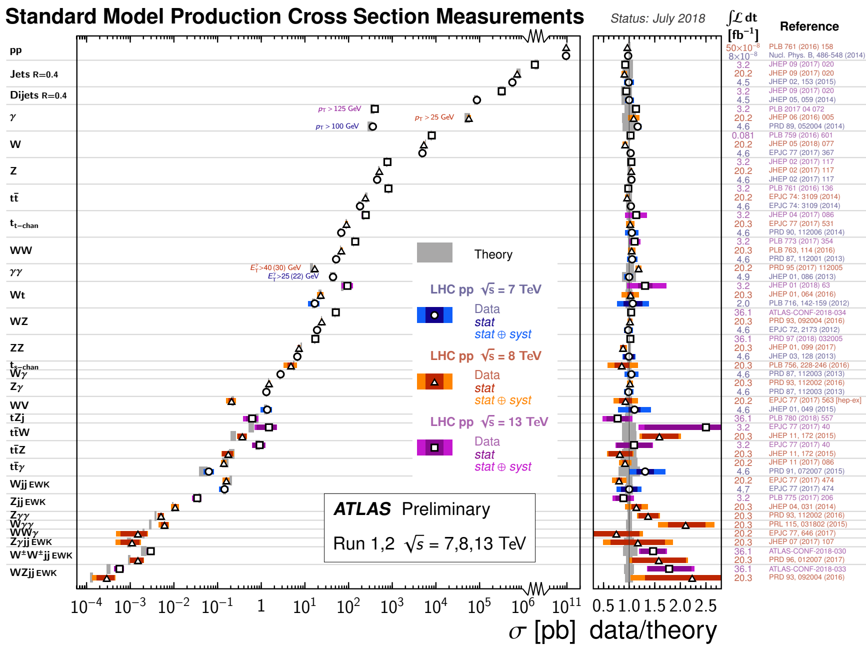

Figure 2.1: Summary of several Standard Model total and fiducial production cross section measurements, corrected for leptonic branching fractions, compared to the corresponding theoretical expectations. All theoretical expectations were calculated at NLO or higher. The dark-color error bar represents the statistical uncertainty. The lighter-color error bar represents the full uncertainty, including systematics and luminosity uncertainties. The data/theory ratio, luminosity used and reference for each measurement are also shown. Uncertainties for the theoretical predictions are quoted from the original ATLAS papers. They were not always evaluated using the same prescriptions for PDFs and scales. The Wgamma and Zgamma theoretical cross-sections have non-perturbative corrections applied to the NNLO fixed order calculations (PRD 87, 112003 (2013)). Not all measurements are statistically significant yet.

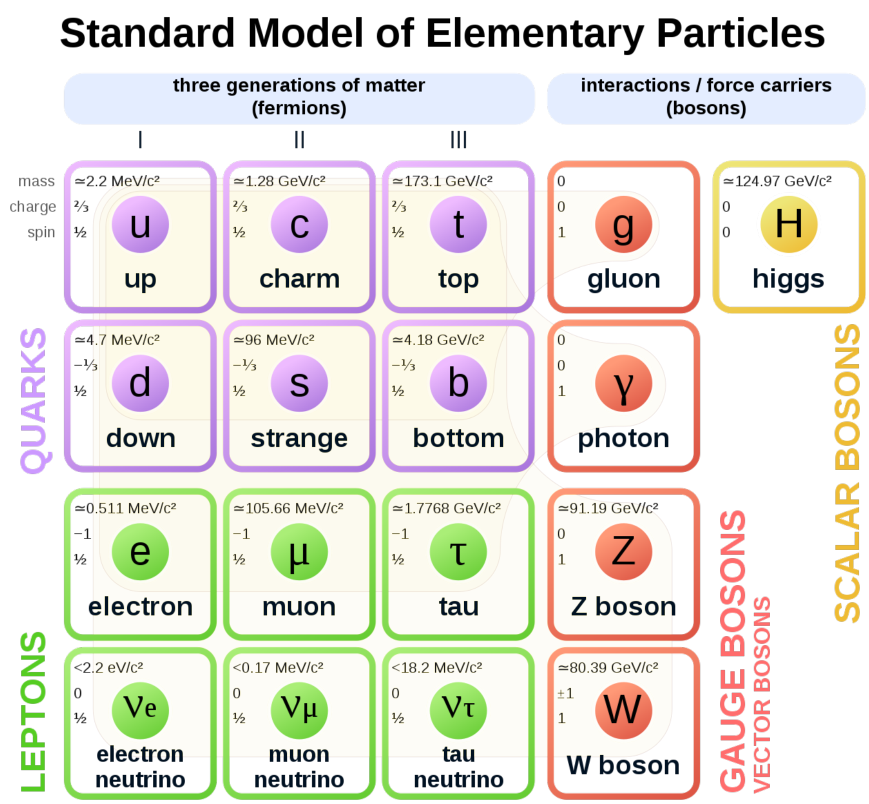

Figure 2.2: Table of all observed fundamental particles of the current Standard Model.

2.1.2 Fermions

These spin-1/2 particles can be further broken up into two distinct familes of particles, the leptons and the quarks, both of which contain three ”generations” each with an ”up” and ”down” type particle. The leptons ”up” type members are the electrically charged electron (e), muon (μ) and tau (τ) while the ”down” type are their electrically neutral counterparts ν_e, ν_μ, ν_τ. The quarks ”up” type members are the up (u), charm (c), and top (t) each with a $+2/3$ elementary charge, while the ”down” type members are the down (d), strange (s), and bottom (b) all of which have a $-1/3$ elementary charge. Each quark carrys a ”color” charge thus allowing them to participate in strong force interactions. Due to the observed color confinement of the strong force these quarks are only observed in colorless bound states known as ”mesons” (1 quark and 1 anti-quark) and ”baryons” (an odd number of quarks and anti-quarks). All of the above fermions have an anti-particle partner which has the opposite electrical charge but is otherwise identical.

2.2 Quantum Electrodynamics

In the SM the Electromagnetic and Weak nuclear forces are unified into the Electroweak interaction which is represented by the $SU(2)_L \times U(1)_Y$ gauge group. The L represents the physical observable that the Weak interaction, and thus the $SU(2)$ transformation, only acts on left handed particle states. The Y states that this is the $U(1)$ symmetry for the weak hypercharge Y instead of the electromagnetic charge. The particle states for these interactions are solutions to the Dirac equation and are represented as Dirac spinor doublets ($\boldsymbol{\Psi_L}$) for the left handed states, and as Dirac spinor singlets (Ψ_R) for the right handed states. Thus when a general transformation from the Electroweak gague group is applied to the left handed spinor doublet you get eq. (2.2)

$$\boldsymbol{\Psi_L} \rightarrow \boldsymbol{\Psi_L'} = exp\left(\underbrace{ig^{'}\frac{Y_L}{2}\zeta(x)}_{U(1)_Y} + \underbrace{ig_W\boldsymbol{\alpha}(x)\cdot\mathbf{T}}_{SU(2)_L}\right)\boldsymbol{\Psi_L}. \tag{2.2}$$

For the right handed spinor singlet the $SU(2)_L$ doesn't contribute and you get eq. (2.3)

$$\Psi_R \rightarrow \Psi_R' = exp\left(\underbrace{ig^{'}\frac{Y_R}{2}\zeta(x)}_{U(1)_Y}\right)\Psi_R. \tag{2.3}$$

We can see that these local gauge transformations have introduced space-time dependant terms $\boldsymbol{\alpha}(x)$ and $\zeta(x)$ into our electroweak Lagrangian. Due to the derivatives contained within the kinetic term of this lagrangian, this new configuration would introduce additional terms, thus violating our required local gauge invariance. Luckily, we can remove these additional terms by replacing the standard derivative (∂_μ) with th covariant derivative (D_μ) as seen in eq. (2.4) for the left handed states and eq. (2.5) for the right handed states.

$$D_\mu = \partial_\mu - \underbrace{\frac{1}{2}ig^{'}B_\mu Y_L}_{U(1)_Y} - \underbrace{\frac{1}{2}ig_W \mathbf{W}_\mu \cdot \boldsymbol{\tau}}_{SU(2)_L} \tag{2.4}$$

$$D_\mu = \partial_\mu - \underbrace{\frac{1}{2}ig^{'}B_\mu Y_R}_{U(1)_Y} \tag{2.5}$$

311 Here we see two new gauge fields; B_μ the weak hypercharge field and $\boldsymbol{W_\mu}$ the charged weak field as well as the associated coupling constants $g^{'}, g_W, Y_L, Y_R$ and the $SU(2)$ generators $\boldsymbol{\tau}$. Next we right down the transformation properies of these new fields

$$\boldsymbol{W}_\mu(x) \to \boldsymbol{W}^{'}_\mu(x) = \boldsymbol{W}_\mu + \partial_\mu \boldsymbol{\alpha}(x) + g_W \boldsymbol{W}_\mu(x) \times \boldsymbol{\alpha}(x) \tag{2.6}$$

$$B_\mu \to B^{'}_\mu = B_\mu + \frac{1}{g^{'}}\partial_\mu \zeta(x) \tag{2.7}$$

The form of these fields is choosen such that the final Lagrangian is invariant under $SU(2)_L \times U(1)_Y$ transformations, and thus we have restored gauge invariance for the kinetic term of our electroweak Lagrangian! Inserting these new definitions into the Lagrangian for the spinor field Ψ which satisfies the free-particle Dirac equation we get

$$\mathcal{L} = i\bar{\boldsymbol{\Psi}}_{\boldsymbol{L}}\gamma^\mu \left(\partial_\mu - \frac{1}{2}ig^{'}B_\mu Y_L - \frac{1}{2}ig_W \mathbf{W}_\mu \cdot \boldsymbol{\tau}\right)\boldsymbol{\Psi}_{\boldsymbol{L}} + i\bar{\Phi}_R\gamma^\mu\left(\partial_\mu - \frac{1}{2}ig^{'}B_\mu Y_R\right)\Phi_R \tag{2.8}$$

Next we must construct the gauge field self interaction and mass terms

$$\mathcal{L} = -\frac{1}{4}\boldsymbol{F}_{\mu\nu}\boldsymbol{F}^{\mu\nu} - \frac{1}{4}B_{\mu\nu}B^{\mu\nu} + \frac{1}{2}M_W^2\boldsymbol{W}_\mu\boldsymbol{W}^\mu + \frac{1}{2}M_B^2 B_\mu B^\mu \tag{2.9}$$

where the field tensors $\boldsymbol{F}^{\mu\nu}$ and $B^{\mu\nu}$ are defined to be

$$\boldsymbol{F}^{\mu\nu} = \partial^\mu\boldsymbol{W}^\nu - \partial^\nu\boldsymbol{W}^\mu + g\boldsymbol{W}^\mu \times \boldsymbol{W}^\nu \tag{2.10}$$

$$B^{\mu\nu} = \partial^\mu\boldsymbol{B}^\nu - \partial^\nu\boldsymbol{B}^\mu \tag{2.11}$$

The field tensor terms in eq. (2.9) are invariant under our gauge transformations, but simply plugging in eq. (2.4) or eq. (2.5) into the mass terms shows that these terms violate gauge invariance thus implying $M_W = 0$ and $M_B = 0$ in direct contradiction of the observed masses of the weak gauge bosons. This issue arises again for fermion mass terms as illustrated below for the elctron field (e) expanded in its chiral basis.

$$m_e\bar{e}e = m_e\begin{pmatrix} e_R^\dagger & e_L^\dagger \end{pmatrix}\begin{pmatrix} e_L \\ e_R \end{pmatrix} = m_e(e_R^\dagger e_L + e_L^\dagger e_R) \tag{2.12}$$

Remembering that the left and right handed spinors of the electroweak interaction transform differently we see that this mixture of right and left fields violates gauge invariance. This again forces us to conclude that $m_e = 0$ in contradiction to the observation that the electron does indeed have mass. As mentioned in section 2.1.1 the resolution to these mass mysteries lies in the Higgs mechanism discussed in section 2.4

2.3 Quantum Chromodynamics

Quantum Chromodynamics is the continuation of the mathematical framework established by Quantum Electrodynamics (section 2.2, this time for the strong force described by the $SU(3)_C$ gauge group where the C represents the ”color” charge of QCD. This color charge doesn’t imply actual visible color, but is useful as an anology to the visible spectrum where a combination of red, green, and blue generates white. For QCD the combination of red, green, and blue color charges results in a colorless object. As mentioned in section 2.1.2 the quarks will contain a color (anti-color) charge represented by a color triplet field which transforms under the general $SU(3)$ transformation as shown here

$$q = \begin{pmatrix} q_r \\ \\ q_g \\ \\ q_b \end{pmatrix} \rightarrow q^{'} = exp\left(ig_s \sum_{k=1}^{8} \eta_k(x) \frac{\lambda_k}{2} \right) q \tag{2.13}$$

Here the λ_k are the generators for $SU(3)$, $\eta(x)_k$ is the space-time dependancy for each generator, and g_s is the strong coupling constant. As with QED, the introduction of these space-time dependant terms introduces new terms into the kinematic portion of the lagrangian thus spoiling our gauge invairance. Again, we introduce a covariant derivative to restore invariance

$$D_\mu = \partial_\mu - i g_s G_\mu^k \frac{\lambda_k}{2} \tag{2.14}$$

Here the G_μ^k are the new fields introduced for the 8 gluons. These new fields transform under $SU(3)$ as shown in eq. (2.15)

$$G_\mu^k \rightarrow G_\mu^{\prime k} = G_\mu^k + \partial_\mu \eta_k(x) + g_s f_{klm} \eta_l(x) G_\mu^m \tag{2.15}$$

Given these definitions we can construct the QCD Lagrangian ($\mathcal{L}_{QCD}$) as shown in eq. (2.16) where the gluon field tensor $G_k^{\mu\nu}$ is the one defined in eq. (2.17)

$$\mathcal{L}_{QCD} = \bar{q}(i\gamma_\mu D^\mu - m_q)q - \frac{1}{4} G_k^{\mu\nu} G_{k\mu\nu} \tag{2.16}$$

$$G_k^{\mu\nu} = \partial^\mu G_k^\nu - \partial^\nu G_k^\mu + g_s f_{klm} G^\mu G_m^\nu \tag{2.17}$$

The strong force is peculiar in that we experimentally observe only colorless objects in the form of bound states of quarks known as hadrons. Qualitatively, when a bound state of quarks (meson or baryon) is given sufficeint energy to separate the strong force dramatically increases in strength. At the point where the objects would separate, and thus no longer be colorless, it becomes energetically favorable to produce a quark/anti-quark pair in a process known as hadronization. In other words, attempting to separate a bound quark state into its colored constituents simply results in new colorless bound states. This requirement of colorless objects by the strong force is known as color confinement. For highly energetic strong interactions at hadron colliders the result is an expanding chain of hadronizing quarks and gluons and their decay products known as a jet.

2.4 The Higgs Mechanism

The Higgs Mechanism is the system by which the gauge bosons and fermions attain mass through the spontaneous breaking of the electroweak symmetry of the Higgs potential. This section will also discuss briefly the couplings of the Higgs boson to massive particles, as well as it's self couplings.

2.4.1 Electroweak Symmetry Breaking

The Higgs field is expressed as a complex doublet, $\mathbf{\Phi}$, and thus has four components as shown in eq. (2.18)

$$\mathbf{\Phi}(x) = \begin{pmatrix} \phi^+ \\ \\ \phi^0 \end{pmatrix} = \frac{1}{\sqrt{2}} \begin{pmatrix} \phi_1(x) + i\phi_2(x) \\ \\ \phi_3(x) + i\phi_4(x) \end{pmatrix} \tag{2.18}$$

The four compoenents of this field each represent a degree of freedom which will be used to give the longitudinal polarizations of the gauge bosons $W^{\pm}, Z$ and the mass of the Higgs boson. The resulting lagrangian for the higgs includes a kinetic term (K) as well as the Higgs potential (V) all of which are invariant under the Electroweak gauge symmetry $SU(2)_L \times U(1)_Y$

$$\mathcal{L}_{\text{Higgs}} = \underbrace{(D_\mu \mathbf{\Phi})^\dagger D^\mu \mathbf{\Phi}}_{\text{K}} - (\underbrace{\mu^2 \mathbf{\Phi}^\dagger \mathbf{\Phi} + \lambda(\mathbf{\Phi}^\dagger \mathbf{\Phi})^2}_{\text{V}}) \tag{2.19}$$

Here we constrain $\mu^2 < 0$ and $\lambda > 0$ such that the potential forms a stable minima. The shape of this potential is shown in fig. 2.3 and is often refered to as the "Mexican-hat" or "Wine-bottle" potential.

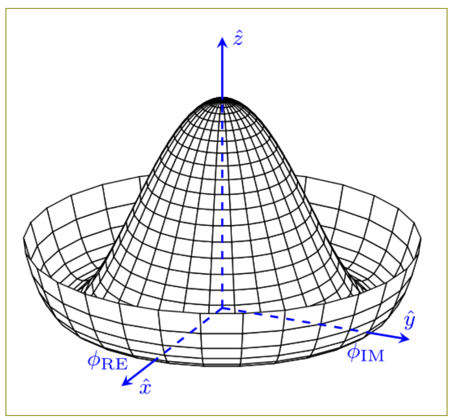

Figure 2.3: A lower dimensionality representation of the shape of the Higgs Potential. The central peak represents a $v = 0$ rotationally symmetric unstable state, while the trough represents the infinite choices of minima that can be selected upon the spontaneous breaking of symmetry.

Whatever you call it, this potential is significant in that its minimum is not at $\mathbf{\Phi} = 0$ but instead is symmetric around the origin thus defining an infinite number of states that minimize V. The value of this minima can be calculated by taking the derivative of V with respect to $\mathbf{\Phi}$ and setting it equal to 0. This value, also known as the vacuum expectation value (vev) has been found to be $v \equiv \sqrt{-\mu^2/\lambda} = 246$ GeV. In order to reach this ground state energy, the Higgs field must spontaneously break this symmetry, and thus aquire an arbitrary single value. For ease of calculation we orient our coordinate system such that

$$\langle \mathbf{\Phi}(x) \rangle = \frac{1}{\sqrt{2}} \begin{pmatrix} 0 \\ v \end{pmatrix} \tag{2.20}$$

Next we parameterize small perturbations around the minimum of the Higgs potential as

$$\langle \mathbf{\Phi}(x) \rangle = \frac{1}{\sqrt{2}} \begin{pmatrix} 0 \\ v + h(x) \end{pmatrix} \exp\left(i \frac{\tau^i}{2} \theta^i(x) \right) \tag{2.21}$$

Here the real scalar field $h(x)$ corresponds to radial perturbations of the minima and while the three $\theta^i(x)$ are the Nambu-Goldstone fields with values determined by your choice of gauge. Choosing the unitary gauge of $\theta^i(x) = 0$ and expanding the kinetic term of eq. (2.19) around the vev we get

$$\mathcal{L}_{\text{Higgs},K} = \frac{g^2v^2}{8}\left((W_\mu^-)^\dagger W^{-\mu} + (W_\mu^+)^\dagger W^{+\mu}\right) + \frac{1}{2}\begin{pmatrix} W_\mu^{3\dagger} & B_\mu^\dagger \end{pmatrix} \boldsymbol{M}^2 \begin{pmatrix} W^{3\mu} \\ B^\mu \end{pmatrix} + \dots \tag{2.22}$$

Here the first term is the physical mass term for the $W^\pm$ bosons where we have constructed their charge eigenstates ouf of the $W^{1,2}$ fields like this $W^\pm = \frac{1}{\sqrt{2}}(W^1 \mp iW^2)$. The second term represents the mixture of the W^3 and B fields through the mass matrix $\boldsymbol{M}$. By diagonalizing this matrix and identifying the mass eigenstates we find the physical fields of the photon (γ) and the Z boson

$$\boldsymbol{M}^2_{Diagonalized} = \begin{pmatrix} 0 & 0 \\ 0 & \frac{v^2}{4}(g_W^2 + g'^2) \end{pmatrix} \tag{2.23}$$

The upper left diagonal element corresponds to the massless photon while the lower right diagonal element gives the mass of the massive Z boson. This leaves us with the following masses for the 4 Electroweak bosons

$$m_W = \frac{1}{2}g_W v \quad , \quad m_Z = \frac{1}{2}v\sqrt{g_W^2 + g'^2} \quad , \quad m_\gamma = 0 \tag{2.24}$$

The masses of the $W^\pm$ and Z gauge bosons can be related through the Wineberg angle or mixing angle which

$$\theta_W = cos^{-1}\left(\frac{g_W}{\sqrt{g_W^2 + g'^2}}\right) \rightarrow m_Z = \frac{m_W}{cos\theta_W} \tag{2.25}$$

Using this definition we can write out the exact mixture of B and W^3 that make up the photon and Z boson

$$\gamma = \cos(\theta_W)B + \sin(\theta_W)W^3 \tag{2.26}$$

$$Z = -\sin(\theta_W)B + \cos(\theta_W)W^3 \tag{2.27}$$

2.4.2 Fermion Mass Terms

In section 2.2 we saw that fermion mass terms violate gauge invariance due to the mixing of the left and right chiral states. The Higgs mechanism again allows for a gauge invariant method of generating mass terms but this time through the Yukawa coupling of the Higgs field to the fermion fields. To see an example of this here is the Yukawa coupling term for the electron doublet ($\boldsymbol{\Psi_L}$) and singlet (Ψ_R) coupling to the Higgs field ($\boldsymbol{\Phi}$) after spontaneous symmetry breaking giving it the form shown in eq. (2.21) where we have again choosen the unitary gauge $\Phi^i(x) = 0$.

$$\mathcal{L}_{Yukawa} = -g_e\left[\bar{\boldsymbol{\Psi}}_{\boldsymbol{L}}\boldsymbol{\Phi}\Psi_R + \bar{\Psi}_R\boldsymbol{\Phi}^{\dagger}\boldsymbol{\Psi}_{\boldsymbol{L}}\right] \tag{2.28}$$

$$= -\frac{g_e}{\sqrt{2}}\left[\begin{pmatrix}\bar{\nu}_e & \bar{e}\end{pmatrix}_L \begin{pmatrix}0 \\ \nu + h\end{pmatrix} e_R + \bar{e}_R \begin{pmatrix}0 & (\nu + h)\end{pmatrix}\begin{pmatrix}\nu_e \\ e\end{pmatrix}_L\right] \tag{2.29}$$

$$= -\underbrace{\frac{g_e}{\sqrt{2}}}_{m_e}\nu\left(\bar{e}_L e_R + \bar{e}_R e_L\right) - \underbrace{\frac{g_e}{\sqrt{2}}}_{g_{e,h}} h\left(\bar{e}_L e_R + \bar{e}_R e_L\right) \tag{2.30}$$

And voila, we have successfully generated mass terms for our fermion field and maintained the gauge invariance of our Lagrangian by using all gauge invariant fields. This operation has also left us with the second term which represents the coupling of the elctron to the higgs itself thus giving us the form of it's coupling constant $g_{e,h}$. Using our newly found mass of the electron m_e we can write

$$g_{e,h} = \frac{g_e}{\sqrt{2}} = \frac{m_e}{\nu} \tag{2.31}$$

Thus we see that the coupling of the higgs boson to a fermion is indeed proportional to the mass of the fermion itself. In other words, the more massive a particle is, the more the higgs couples to it and vice versa.

2.4.3 The Higgs Boson

As we have seen this Higgs mechanism not only properly mixes the gauge fields thus providing them gauge invariant mass terms, it also properly combines the left and right chiral states of fermions to produce their mass terms. The final step then is to determine an observable of the theory that can be tested in experiment, namely the existence of a massive scalar particle, the Higgs boson intself.

Turning our attention to the potential term (V) of eq. (2.19) and substituting in our definition for $\mathbf{\Phi}$ given in eq. (2.21) we find

$$\mathcal{L}_{\text{Higgs,V}} = \frac{1}{2}\mu^2\nu^2 - \mu^2 h^2 + \lambda\nu h^3 + \frac{1}{4}\lambda h^4 \tag{2.32}$$

Here the first term is constant and thus can be ignored. The second term is the mass term for the SM particle the Higgs boson, $m_h = \sqrt{-2\mu^2} = \sqrt{2\lambda}\nu$. Remembering that $h = h(x)$ was used for small radial petrubrations of the Higgs field we can identify the Higgs boson simply as an excitation of the Higgs field. Finally, the third and fourth terms represent the Higgs boson self-couplings. With these couplings and mass terms in hand we can now move on to the experimental verification of this theory as discussed next in chapter 3.

Chapter 3

Boosted Higgs at the LHC

In chapter 2 I've shown how the higgs mechanism resolves inconsistencies of the model surrounding the generation of gauge boson and fermion mass terms while also maintaining gauge invariance. However to understand the search for and resulting discovery of this SM Higgs boson requires the discussion of how one goes about producing and detecting the physical object itself. In order to gather sufficient statistics to validate the theory we require a collider capable of putting enough energy into a collision to rapidly produce Higgs bosons for study. To this end the Large Hadron Collider (LHC) discussed in chapter 4 was laboriously designed, funded, and constructed by the largest international collaboration of scientists on the planet. In this chapter I will discuss the relevant Higgs boson production mechanisms available at the LHC as well as the various decay modes of the Higgs that were used for its discovery, and are currently used to measure its properties.

3.1 Higgs Production Mechanisms

At the LHC the dominate production mechanisms for the higgs in order of decreasing cross section are: gluon-fluon fusion (ggF), vector boson fusion (VBF), vector boson associated production or “Higgsstrahlung” (VH), and associated production with $t\bar{t}$ ($t\bar{t}H$) and $b\bar{b}$ ($b\bar{b}H$). The cross sections with associated theoretical uncertainties for each is shown as a function of the center of mass energy $\sqrt{s}$ in fig. 3.1 and the actual feynman diagrams can be seen in fig. 3.2. For reference the exact produciton cross sections for a variety of center of mass energies are detailed in table 3.1.

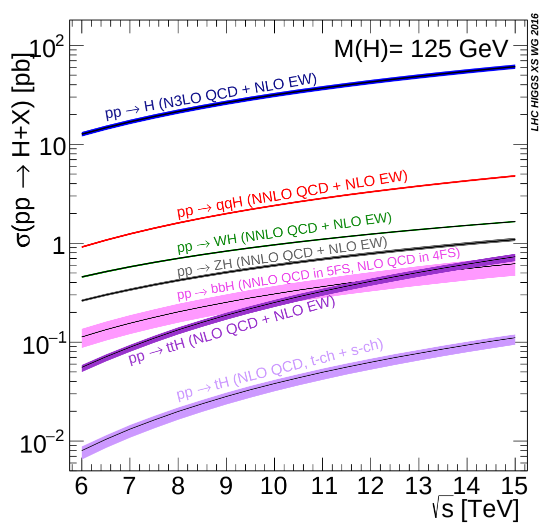

Figure 3.1: Cross section for the production of the SM Higgs boson as a function of the center of mass energy ($\sqrt{s}$) at the LHC. [1]

The dominant Higgs production mechanism at hadron colliders is ggF. This may seem strange as gluons are massless and thus do not couple directly to the Higgs. Instead the

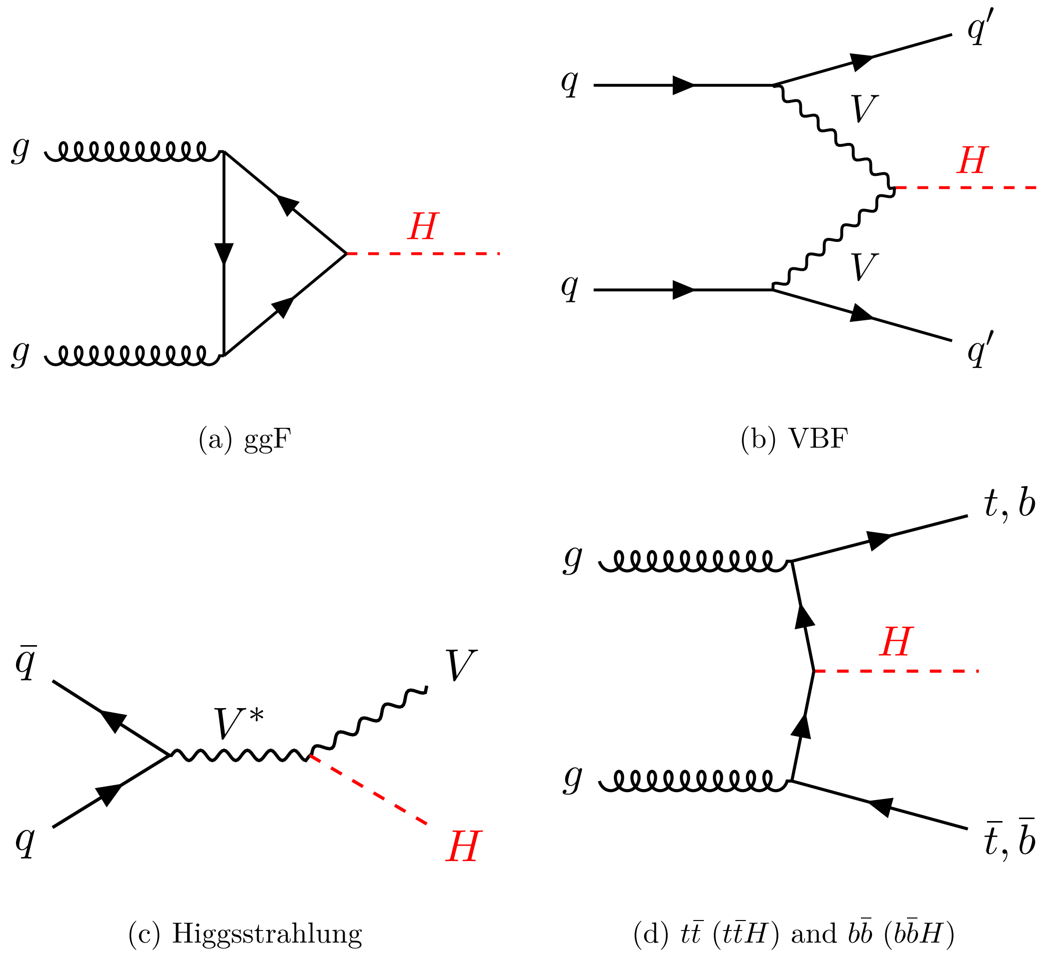

(a) ggF

(b) VBF

(c) Higgsstrahlung

(d) $t\bar{t}$ ($t\bar{t}H$) and $b\bar{b}$ ($b\bar{b}H$)

Figure 3.2: Feynman diagrams representing the dominant Higgs production modes at the LHC.

Table 3.1: SM Higgs boson production cross sections in units of pb for $m_H = 125$ GeV in pp collisions as a function of the center-of-mass energy, $\sqrt{s}$, at the LHC. The predictions for the ggF channel include the latest N3LO results leading to reduced theoretical uncertainties by a factor around 2 compared to the N2LO results [1].

$\sqrt{s}$ (TeV)	ggF	VBF	WH	ZH	$t\bar{t}H$	Total (pb)
8	$21.4^{+5\%}_{-5\%}$	$1.60^{+2\%}_{-2\%}$	$0.70^{+3\%}_{-3\%}$	$0.42^{+5\%}_{-5\%}$	$0.13^{+8\%}_{-13\%}$	24.2
13	$48.6^{+5\%}_{-5\%}$	$3.78^{+2\%}_{-2\%}$	$1.37^{+2\%}_{-2\%}$	$0.88^{+5\%}_{-5\%}$	$0.50^{+9\%}_{-13\%}$	55.1
14	$54.7^{+5\%}_{-5\%}$	$4.28^{+2\%}_{-2\%}$	$1.51^{+2\%}_{-2\%}$	$0.99^{+5\%}_{-5\%}$	$0.60^{+9\%}_{-13\%}$	62.1

gluons indirectly couple to the Higgs via a quark loop. As discussed in section 2.4.2, the coupling of a fermion is proportional to m_f so the dominant contribution to this quark loop comes from the top quark.

The second largest cross section for Higgs production at the LHC comes from the VBF mechanism. In VBF the initial state quarks scatter via the exchange of a $W^{\pm}$ or Z boson which subsequently radiates the Higgs boson. Unlike ggF this production mechanism scatters the initial state quarks which allows them to be observed as part of the interaction. The existence of these extra quarks makes these interactions easier to select for during analysis.

Next we have Higgs production in association with a vector boson. The cross section for this is even lower than the above two, but remains important due to the easily selected signature of the decaying vector boson. The largest background at the LHC is multijet events coming from interactions that produce strong force objects. Thus the leptons from the boson's decay act as a discriminator from this multijet background greatly reducing its effect on sensitivity.

With the lowest cross section of the four methods discussed we have the production of the Higgs in assocaiation with either $b\bar{b}$ or $t\bar{t}$. This channel is important due to our ability to measure not only the Higgs, but also the quarks that it directly coupled with. This allowes us to directly measure the coupling of the Higgs to that quark, unlike the ggF method where the quark in the loop is never directly observed.

As we can see, each of these methods has its advantages and disadvantages as well as different valuable information that can be extracted. The result is a need for many different analysis using different techniques to search for each mechanism.

3.2 Parton Distribution Function

The LHC collides protons, however looking at the feynman diagrams in fig. 3.2 we see that it is quarks and gluons (a.k.a partons) that produce these fundamental interactions. This is an indicator that when we calculate the production cross section for a process at the LHC, we have to not only consider the hard-scatter probability of the specific diagram, but also consider the composition of the proton itself. Specifically, we must consider the fraction of the total momentum of the proton held by each of its constituent partons. This concept is described by Parton Distribution Functions (PDFs) which give the probability that the indicated parton carries momentum fraction x of the proton when probed at with energy scale Q. An example PDF for $Q = 10\mathrm{GeV}^2$ and $Q = 10^4\mathrm{GeV}$ in fig. 3.3

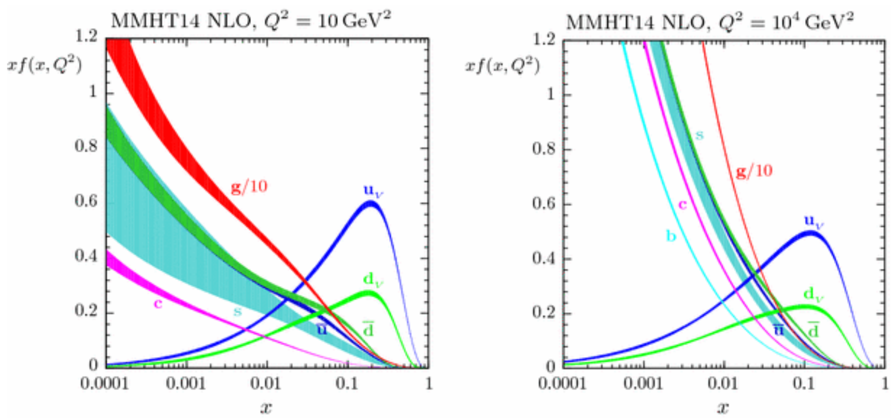

Figure 3.3: [2] MMHT2014 NNLO PDFs at $Q2 = 10\mathrm{GeV}^2$ and $Q2 = 10^4\mathrm{GeV}^2$ with associated 68% confidence-level uncertainty bands. The colored regions indicate the probability of finding the labeled parton with a momentum fraction given along the x axis. As expected the u_V and d_V contain the largest fraction of the momentum, however we can also see that many gluons will exist with smaller fractions of the total momentum. Note that as Q^2 increases you are more likely to find something besides a u/d

3.3 Branching Ratios

The coupling of the SM Higgs with the gauge bosons and fermions has been shown to give these particles their mass, however it also means that the Higgs can decay into all of these particles. In order of most to least likely final states of a Higgs decay we have the decay to; a pair of b-quarks ($b\bar{b}$), a pair of weak vector bosons where one is off-shell (VV^*), two gluons (gg), a duo of tau leptons ($\tau^+\tau^-$), or a pair of photons ($\gamma\gamma$). Similar to the ggF production mechanism discussed in section 3.1 the decays to massless gauge bosons (photons and gluons) are facilitated through loops of massive particles. The exact feynman diagrams depicting the above process' are shown in fig. 3.4 while information about their branching ratios is detailed in table 3.2.

Table 3.2: The branching ratios and the relative uncertainty for a Standard Model Higgs boson with $m_H = 125$ GeV [1].

Decay Channel	Branching Ratio	Relative Uncertainty
$H \to b\bar{b}$	5.84×10^{-1}	$^{+3.2\%}_{-3.3\%}$
$H \to W^+W^-$	2.14×10^{-1}	$^{+4.3\%}_{-4.2\%}$
$H \to \tau^+\tau^-$	6.27×10^{-2}	$^{+5.7\%}_{-5.7\%}$
$H \to ZZ$	2.62×10^{-2}	$^{+4.3\%}_{-4.1\%}$
$H \to \gamma\gamma$	2.27×10^{-3}	$^{+5.0\%}_{-4.9\%}$
$H \to Z\gamma$	1.53×10^{-3}	$^{+9.0\%}_{-8.9\%}$
$H \to \mu^+\mu^-$	2.18×10^{-4}	$^{+6.0\%}_{-5.9\%}$

In table 3.2 the order is determined by two distinct effects; the proportionality of the Higgs couplings to the mass of the decay product, and whether or not the rest mass of the higgs is sufficient to produce the two final state objects. In fig. 3.5 you can see that as the mass of the higgs boson gets closer to $2m_W$ the cross section for $H \to WW$ grows.

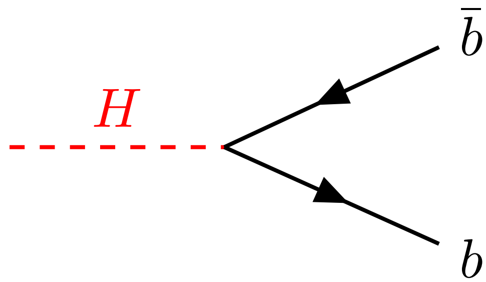

(a) $H \to b\bar{b}$

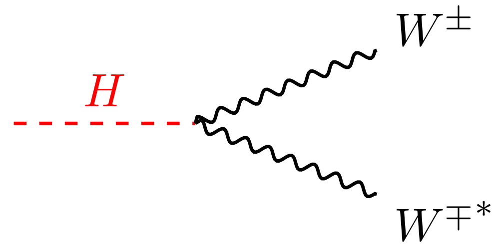

(b) $H \to W^{\pm}W^{\mp *}$

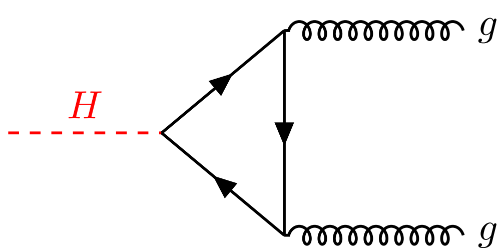

(c) $H \to gg$

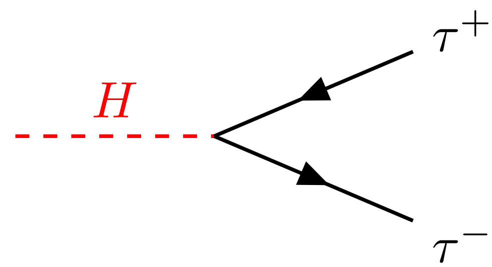

(d) $H \to \tau^{+}\tau-$

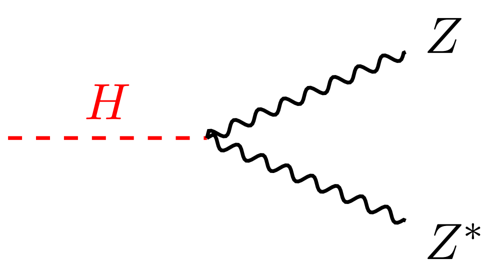

(e) $H \to ZZ^{*}$

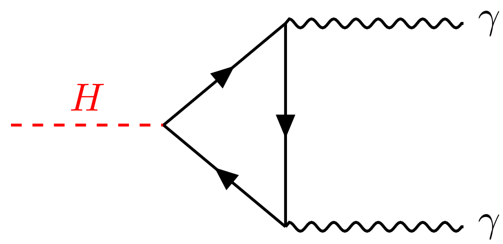

(f) $H \to \gamma\gamma$

Figure 3.4: Feynman diagrams representing the leading Higgs decay channels.

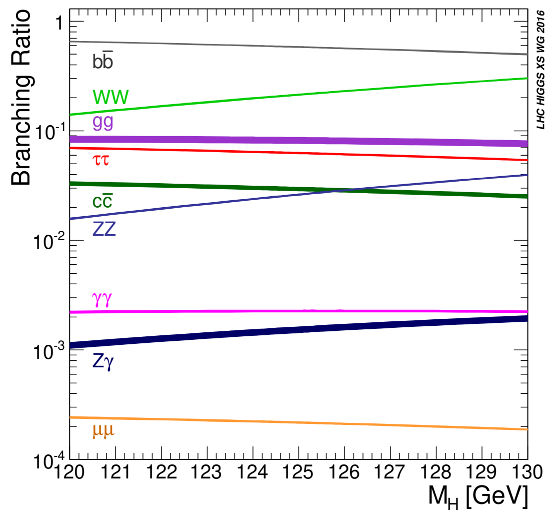

Figure 3.5: Branching ratios for the decay of the SM Higgs boson near $m_H = 125\text{GeV}$ including theoretical uncertainty bands [1]

3.4 Evidence for the SM Higgs

Using the above information about predicted final states the CMS and ATLAS experiment collaborations analyszed 5 fb^{-1} of LHC Run 1 data [3] to make measurements of the SM Higgs production cross-sections and branching ratios. The combined results of these studies can be seen in fig. 3.6 fig. 3.7 and fig. 3.8. Given the uncertanties on the measurements these results show good agreement between the predictions of the Standard Model and experiment with all best fit values falling within 2σ of the SM theoretical prediction.

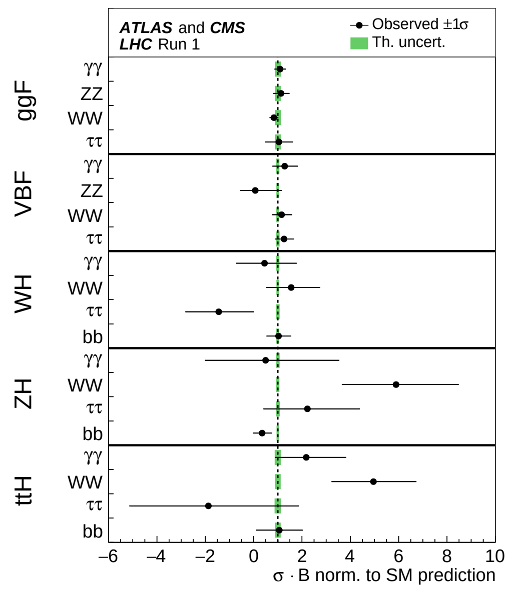

Figure 3.6: Best fit values of $\sigma_i \cdot B^f$ for each specific channel $i \to H \to f$, as obtained from the generic parameterisation with 23 parameters for the combination of the ATLAS and CMS measurements. The error bars indicate the 1σ intervals. The fit results are normalised to the SM predictions for the various parameters and the shaded bands indicate the theoretical uncertainties in these predictions. Only 20 parameters are shown because some are either not measured with a meaningful precision, in the case of the $H \to ZZ$ decay channel for the WH, ZH, and $t\bar{t}H$ production processes, or not measured at all and therefore fixed to their corresponding SM predictions, in the case of the H $\to$ bb decay mode for the ggF and VBF production processes [3].

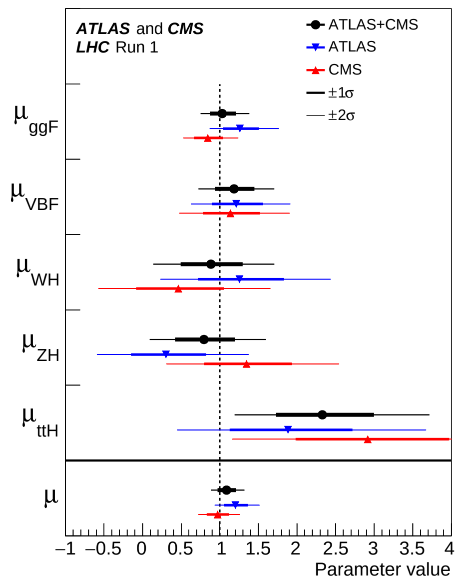

Figure 3.7: Best fit results for the production signal strengths for the combination of ATLAS and CMS data. Also shown are the results from each experiment. The error bars indicate the 1σ (thick lines) and 2σ (thin lines) intervals. The measurements of the global signal strength μ are also shown [3].

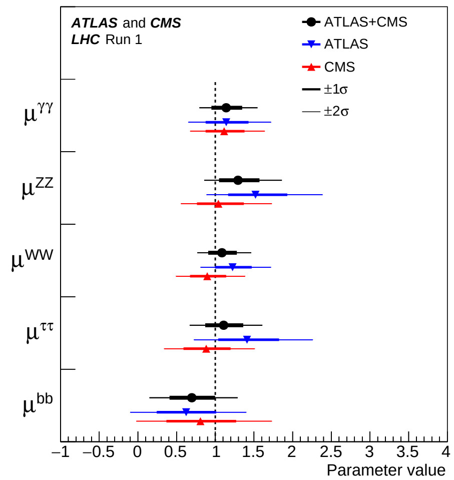

Figure 3.8: Best fit results for the decay signal strengths for the combination of ATLAS and CMS data. Also shown are the results from each experiment. The error bars indicate the 1σ (thick lines) and 2σ (thin lines) intervals [3].

3.5 Boosted Higgs

The strong agreement between the theoretical predictions of the SM Higgs boson and experiment shown in section 3.4 represents the fulfillment of a generation of incredible technological and theoretical achievement. The next step is to push the search for deviations from the model that might hint at the physics of mysteries like the matter / anti-matter asymmetry of the universe, dark matter, the particle nature of gravity and dark energy. One such avenue for search comes in the transfer of large ammounts of momenum in massive particle loops like that of the ggF Higgs production mechanism. By more accurately measuring the couplling of the Higgs to the quarks in these loops, we not only increase our confidence in the SM, we are also gain access to this possible new physics. To this end, and for the purposes of suppresing the QCD multijet background, a study of Boosted Higgs production was undertaken and is discussed further in part III.

Part II

Experimental Apparatus and Associated Facilities

Chapter 4

The Large Hadron Collider

Located 100 meters under the Swiss / French border lies the 26.7 kilometer circumference Large Hadron Collider (LHC) [4]. The culmination of a huge international collaboration, this apparatus is used to produce proton and heavy ion collisions for observation by the four major experiments at the LHC: ATLAS, CMS, LHCb, and ALICE. The system was designed for a maximum center-of-mass energy of $\sqrt{s} = 14$ TeV and a peak instantaneous luminosity of $L = 10^{34}\text{cm}^{-2}\text{s}^{-1}$.

The first LHC workshop was held in 1984 in Lausanne at the European Organization for Nuclear Reserach (CERN) [5]. The nearly 30 year old case for a machine that would push towards the discovery of the elusive Higgs Boson was presented using the existing CERN accelerator facilities and the Large Electron Positron (LEP) collider tunnel. The proposal became reality on September 10, 2008 when the first proton beams were circulated, only to have calamity strike 9 days later in the form of a catastrophic electrical fault. The repairs and improvements lasted until November 2009 when the LHC restarted. Since then, this modern marvel has worked wonderfully and, as hoped, lead to the discovery of the Higgs Boson by the ATLAS and CMS collaborations July 4, 2013.

The following chapter provides a brief introduction to the worlds most powerful accelerator starting with the little red bottle of hydrogen in building XXX, and ending with the interaction point where protons collide at the highest energies ever produced.

4.1 Particle Injection Chain

We begin with the most common element in the Universe, hydrogen, as our source of protons. A bottle of hydrogen gas provides 100 microsecond pulses of raw H_2 which is then injected into a Duoplasmatron. There, a strong electric field and free elctrons from a cathode ionize the molecule into bare H^+ aka a proton! These protons are then accelerated by a 90kV electric field, leaving the Duoplasmatron at 1.4% the speed of light (~4000km/s) or, in Particle Physics units, about 83KeV. The bare protons are then fed into the accelerating Radio Frequency (RF) cavities of Linear Accelerator 2 (LINAC2). Inside, conductors charged by a powerful oscillating electromagnetic field accelerate the protons to an energy of 50MeV. Along the way, small quadrupole magnets shape the proton bunch ensuring they remain in a tight beam. This pattern of acceleration with RF cavities and shaping/tuning with magnets is then repeated with CERN's first

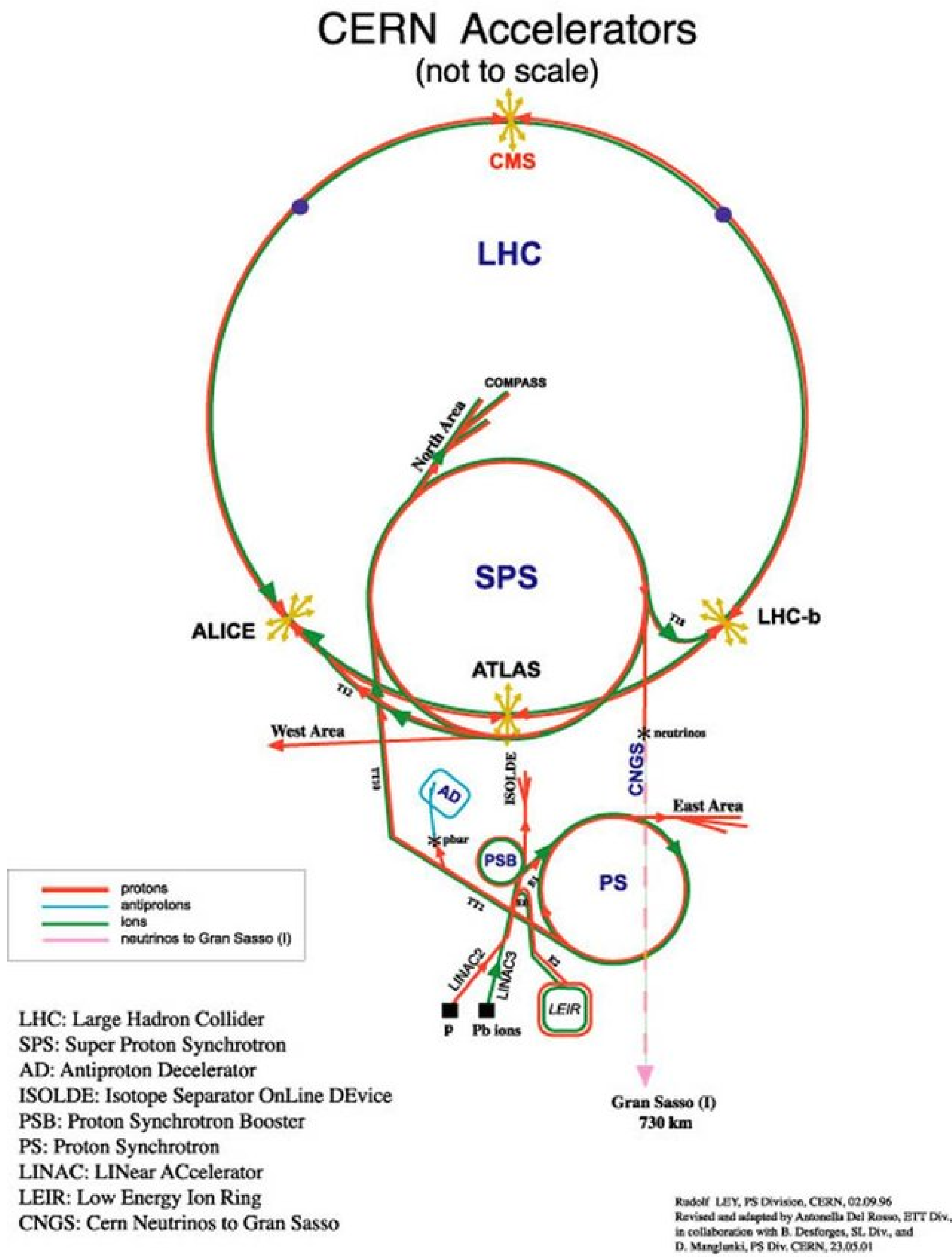

Figure 4.1: CERN accelerator complex

synchrotron, the Proton Synchrotron (PS) rendering a 1.4 GeV proton beam. The final step before the LHC comes with the Super Proton Synchrotron where the same technologies are implemented to produce 450 GeV protons, ready for injection into the LHC. A diagrammatic representation of this chain can be seen in fig. 4.1.

In order to produce proton-proton collisions, the LHC uses two beams circulating in opposite directions. The beams are not continuous, but instead consist of bunches of $\mathcal{O}(10^{11})$ protons with a spacing of 25ns. Given the LHC circumference this allows for 3564 bunches, however only 2808 are filled per beam due to safety requirements and injection limitations. Each beam takes 4 minutes and 20 seconds to fill and then an additional 20 minutes to for the protons to reach their maximum energy of 7 TeV, or 99.99999991% the speed of light! Under normal operating conditions these beams can be used for many hours.

4.2 LHC Layout and Design

While often depicted as a perfect circle the LHC is in reality an octagon with rounded edges, called arcs, as can be seen in fig. 4.2. Here you can see the counter circulating beams of protons depicted in red and blue. These beams are focused and collided at the 4 dedicated interaction points at rates of up to 40 MHz. Two of these points are occupied by the ATLAS and CMS experiments, both of which are high luminosity, multi-purpose experiments.

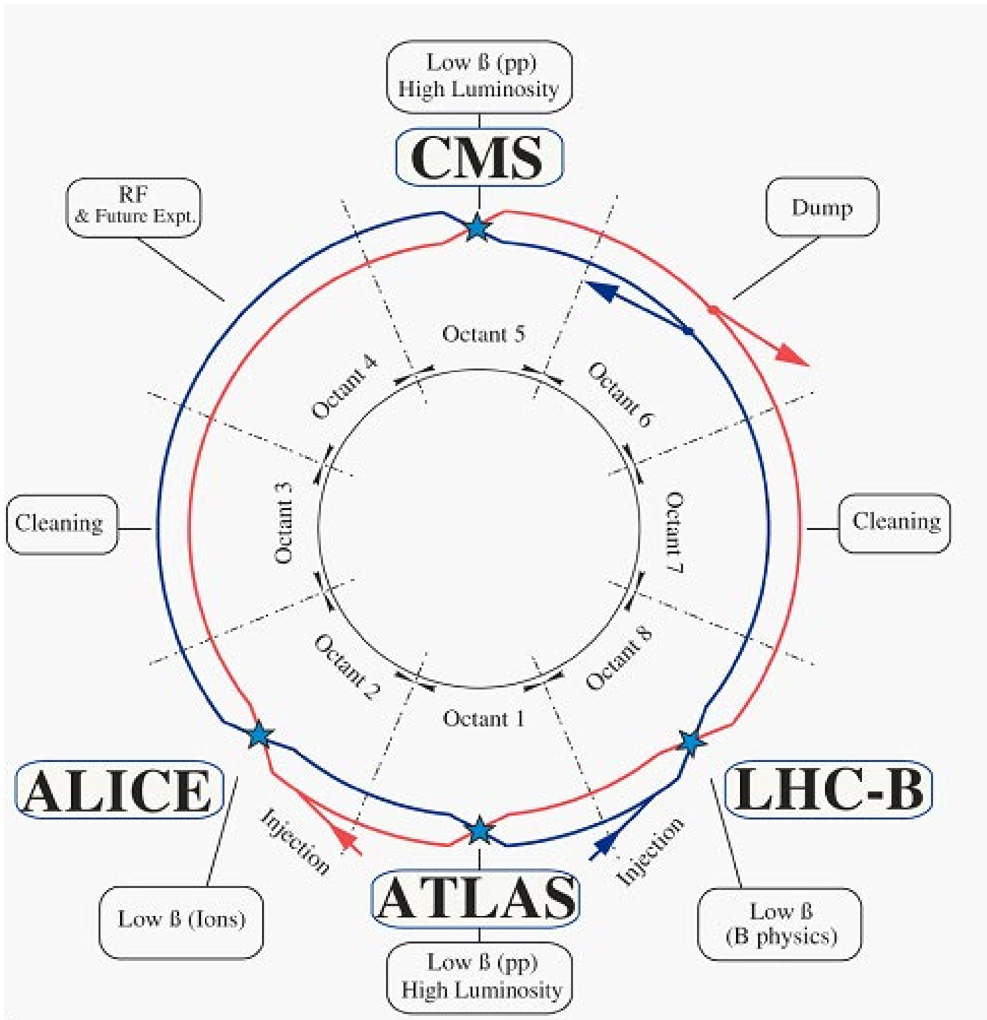

Figure 4.2: Labeled diagram of all the experiments at the LHC indicating the counter circulating beams and points of interest along the circumference of the accelerator.

The exact design of the LHC tunnel is due to the experimental constraints of the original machine for which it was built, the Large Electron Positron (LEP) Collider. For the $\sim 2,000$ times lighter electron the maximum energy was limited by the synchrotron radiation, proportional to $\frac{1}{m^4}$, requiring long straight sections of accelerating RF cavities to recuperate the lost energy. Given that this effect is $\mathcal{O}(10^{13})$ times smaller for the proton the LHC is instead limited by our ability to design and construct magnets strong enough to bend the beam given the already determined curvature of the 8 arcs.

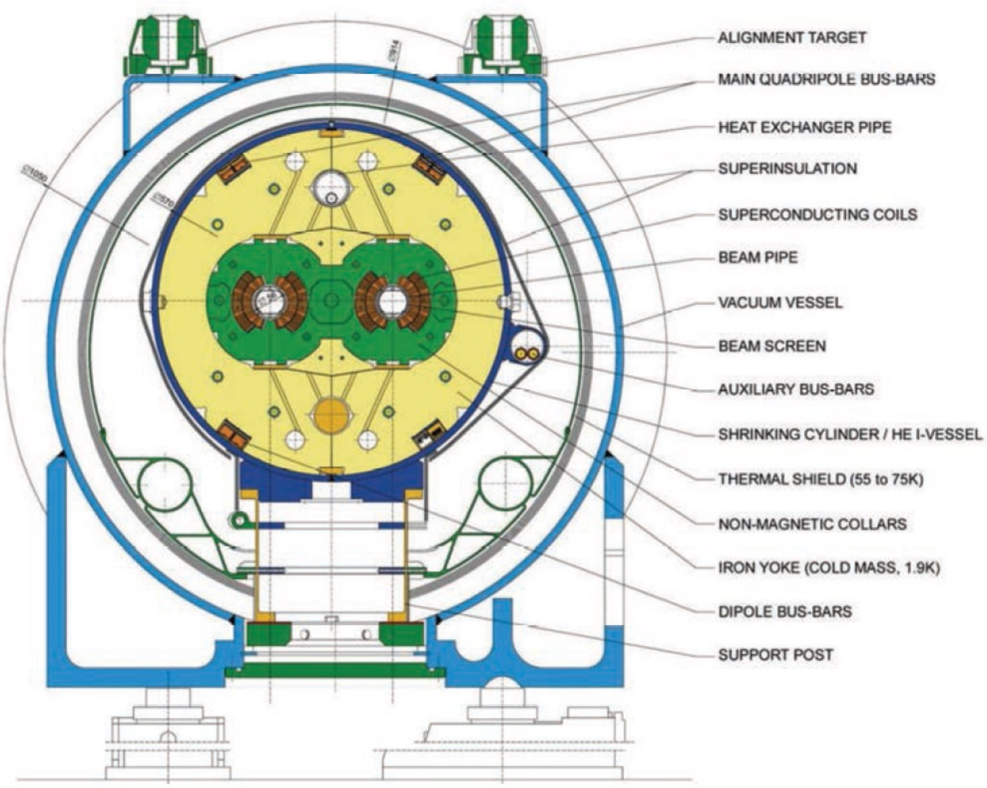

Figure 4.3: Depiction of a LHC dipole magnet 2-in-1 design labeling the major components

The oppositely circulating beams must each have their own ring and magnetic field which lead to the creation of a twin-bore (i.e. ”two-in-one”) magnet design, a cross section of which can be seen in fig. 4.3. These magnets are constructed using NbTi superconductors which are cooled to 2K using superfluid helium. These magnets are designed to provide the needed 8.33 T magnetic field required to bend the proton trajectories at the designed beam energy of 7 TeV. In total 1231 of these 15 m bending dipole magnets are used, in association with 392 5-7m quadrupole magnets which are responsible for keeping the proton bunches in a tight beam by squeezing them both horizontally or vertically.

4.3 Performance

Since the begining of its stable running in 2010 the LHC has performed well, exceeding expectations. While the experiment itself is incredibly complex, the performance of the machine, for the purposes of our analysis, can be reduced to two numbers; the familiar center of mass energy of the beams and a less common quantity known as the integrated luminosity.

For particle physics the integrated luminosity is proportional to the total number of collisions recorded during a specified time period, while the instantaneous luminosity is proportional to the bunch crossing rate along with the cross section of a proton-proton interaction and represents the potential number of collisions per second. Knowing this we can see that the integrated luminosity, L_{int} is simply the integral of the instantaneous luminosity $L_{inst.}$ for a choosen data period as seen in eq. (4.1).

$$L_{int} = \int L_{inst.} dt \tag{4.1}$$

For a standard Gaussian beam, $L_{inst.}$ can be written as

$$L_inst = \frac{N_b^2 n_b f_{rev} \gamma_r}{4\pi \epsilon_n \beta^*} F \tag{4.2}$$

where N_b is the number of particles per bunch, n_b the number of bunches per beam, f_{rev} the revolution frequency, γ_r the relativistic gamma factor, ϵ_n the normalized transverse beam emittance, β^* the beta function at the collision point, and F the geometric luminosity reduction factor due to the crossing angle at the interaction point given by

$$F = \left(1 + \left(\frac{\theta_c \sigma_z}{2\sigma^*}\right)^2\right)^{-1/2} \tag{4.3}$$

where θ_c is the full crossing angle at the interaction point, σ_z is the RMS bunch length, and σ^* is the transverse RMS beam size at the interaction point.

For the ATLAS experiment the integrated luminosity for each year can be seen in fig. 4.4a as well as an example of the instantaneous luminosity for the choosen year in fig. 4.4b.

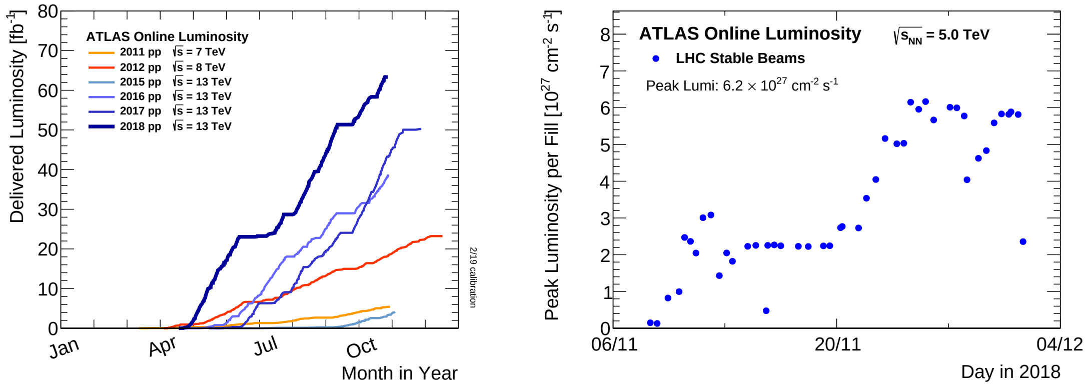

(a) Integrated Luminosity 2011 - 2018 (b) 2018 Peak Instantaneous Luminosity

Figure 4.4: Luminosity is monitored as both a running total known as the Integrated Luminosity as depicted in (a) and as an instantaneous quanity as shown in (b).

4.4 Pile-up at the LHC

Given the large number of protons per bunch and the cross-section of a proton-proton interaction, the probability to observe multiple interactions per bunch crossing is quite high. These multiple-interaction are known as pile-up, μ or the time-averaged representation $\langle\mu\rangle$, and comes in two different forms:

1. **In-time pile-up:** These are the other proton-proton collisions that occur during the same bunch crossing as the primary interaction that cauesd the Data Aquisition (DAQ) system to trigger. These are the standard extra interactions we expect to observe as stated above.

2. **Out-of-time pile-up:** These are interactions that occur either before or after a

bunch crossing that causes the DAQ to trigger. This effect is generally due to the long integration times of some detector electronics.

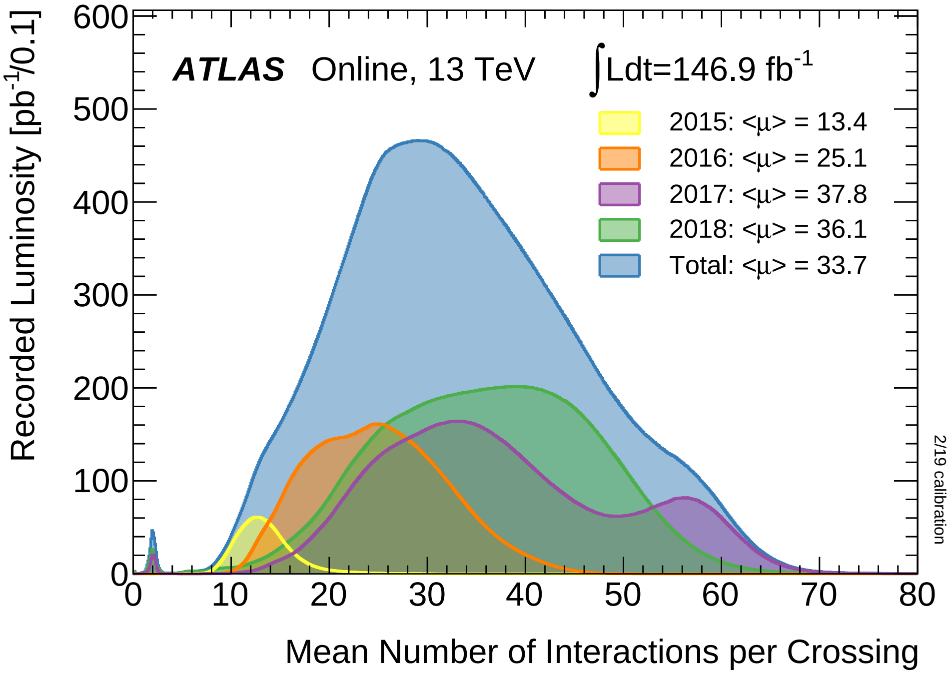

Figure 4.5: Pileup for data taking periods 2015 - 2018

The pile-up profile for past years can be seen in fig. 4.5. The width of this distributino is due a combination of Poisonian statistics, the decrease in number of protons per bunch over the lifetime of a single run, and optimization tweaks to the beam's profile during the LHC's operation. Understanding and eliminating the noise from these pile-up events is crucial to reconstructing physics variables that describe the primary interaction we aim to observe.

Chapter 5

The ATLAS Detector

Given the immense energies available at the LHC, and the veritable zoo of paricles we are trying to detect, we require a general-purpose experiment in order to fully exploit the full range of physics opportunities provided. Two international collaborations rose to this challenge, the CMS (Compact Muon Solenoid) and ATLAS (A Toroidal LHC ApparatuS) experiments. While both have similar physics goals and each of them strengths and weaknesses, this dissertation will focus on the ATLAS experiment and the intricacies of its three sub-detectors and two massive magnet systems depicted in fig. 5.1.

Originally proposed in 1994, the ATLAS detector was completed in 2008. On July 4th, 2012 in a joint announcement the ATLAS and CMS experiments presented the discovery of the long predicted Higgs Boson. The ATLAS collaboration now boasts over 3000 physicists from 175 institutions spread across 38 countries and continues to

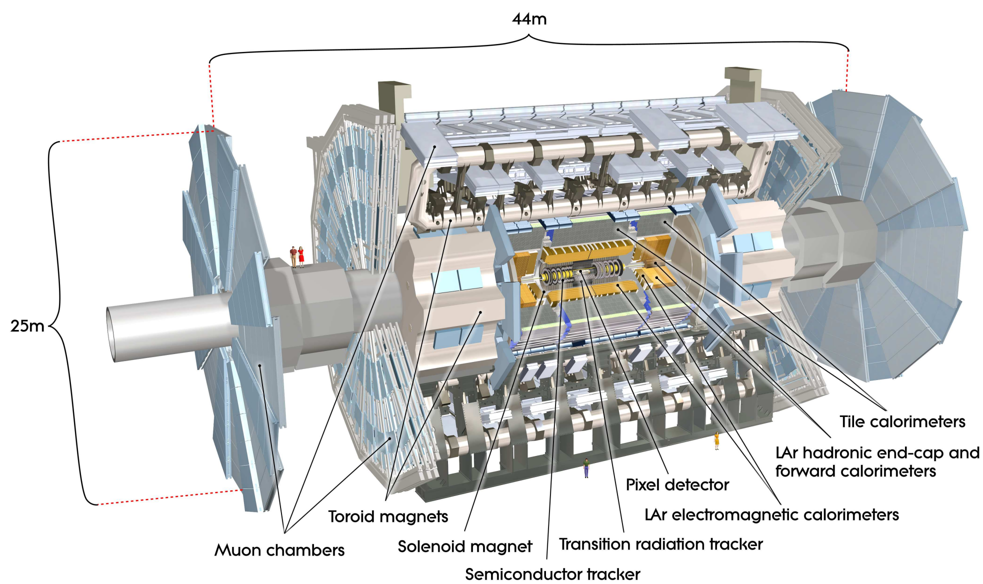

Figure 5.1: [6] Here we see a cut-away side view of the ATLAS detector with the major components labeled. Note that within each of these labeled components there may exist multiple different detector technologies. For scale two people in red are shown standing between the disk muon chambers on the left side of the figure.

probe the limits of the Standard Model in pursuit of answers to some of humanity's deepest questions.

Located approximately 100 meters underground in a vast excavated chamber, the ATLAS detector rests its 7000 metric tons on a bed of concrete-reinforced steel. Out of it flows the signals from 100 million electronic channels through a zip-tied mass of 3000+ kilometers of cabling. At its very center is one of the four interaction points of the LHC, specifically Point 1, where the two counter circulating proton beams are shaped and then brought together by a series of magnets. The energetic particles resulting from this collision then fly out in all directions into the bulk of the ATLAS detector.

The first sub-system they meet is the Inner Detector (ID) and its many layers of strip and pixel silcon detectors along with a transition radiation gaseous wire detector, all bathed in the 2T mangnetic field from the surrounding superconducting solenoidal magnet. This system exploits the ionization of charged particles to track their curved trajectory through the magnetic field. This curvature gives us charge information, a momentum measurement, and precisely-located 3D vertices crucial to the identification of the secondary vertices of a B-hadron decay.

Outside of the solenoid the particles encounter the Electromagnetic and then the Hadronic sampling calorimeters. Here, layers of scintillator and high radiation length materials are implemented to measure the energy of electrons, photons, and hadrons. As the goal is to completely absorb the energy of all outgoing particles the calorimeter has a nearly 4π solid angle coverage.

Finally we have the muon system surrounding the calorimeter and equipped with its own toroidal magnet system. Here the charged muon bends in the magnetic field while leaving a trail of ionization in the Muon Spectrometer before exiting the detector completely. Neutrinos are the only other Standard Model particle that leave the detector, however they do so without detection. A depiction of the various particle interactions with the different detector sub-systems can be seen in fig. 5.2

In the following sections I will explain our chosen coordinate system and give a more detailed review of these three detector sub-systems.

5.1 ATLAS Coordinate System

Using the nominal interaction point as the origin, ATLAS uses a right-handed coordinate system where the positive x-axis points towards the center of the LHC ring, the positive y-axis points upwards, and the positive z-axis is defined by the counter clockwise circulating beam direction as viewed from above shown in fig. 5.3 [6].

Using these coordinates we can define the physical momentum of the objects measured as $\vec{p} = (p_{\mathrm{T}}, p_z)$ with p_{T} being the momentum of the object in the transverse plane and p_z the momentum along the beam axis. Given the cylindrical symmetry of ATLAS it is desirable to define the polar angle θ from the beam axis with the r-ϕ plane being perpendicular to that axis. Since the particles we observe are relativistically boosted in the z-axis it is desirable to use the Lorentz invariant quantity pseudorapidity (η) defined

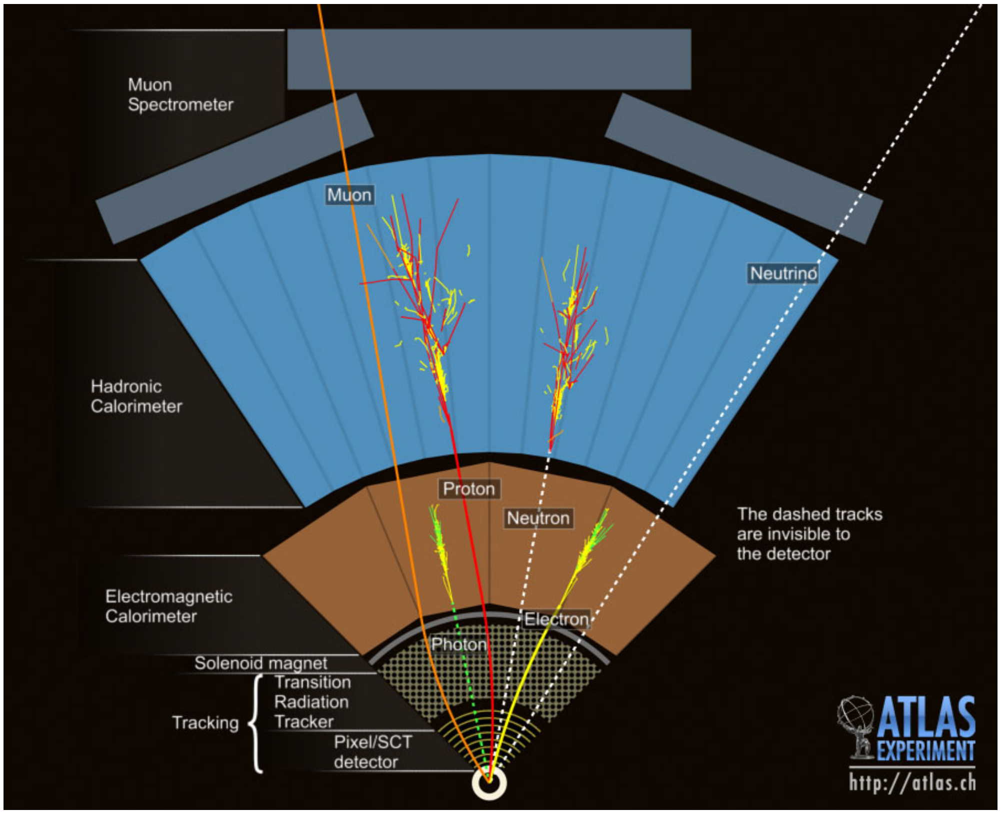

Figure 5.2: This slice of the ATLAS detector depicts how different particles interact with each component of the detector it crosses. A dashed line indicates no interaction while a solid line indicates interaction. Electrons (yellow/green) and charged hadrons (red) interact with the tracker and curve in the solenoid's magnetic field. Electrons and photons (yellow/green) are absorbed by the Electromagnetic calorimeter. All hadrons (red/yellow) are absorbed by the Hadronic calorimeter. The muons (orange) curve in both the solenoid and toroid magnetic fields before exiting the detector. Finally, the neutrinos (white) pass through the entire detector without interacting.

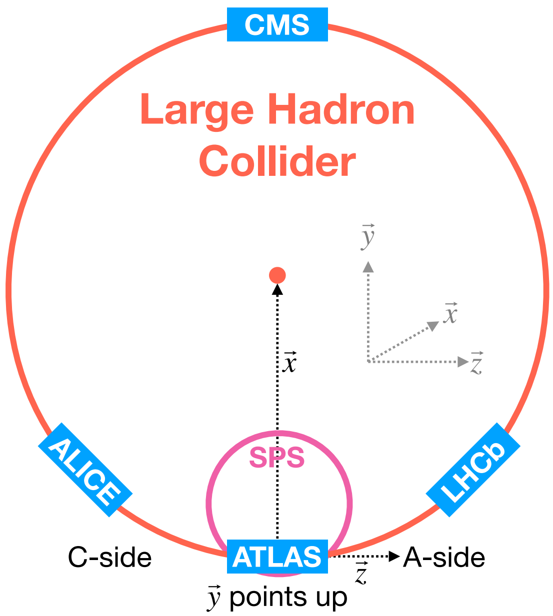

Figure 5.3: [7] A cartoon view of the the LHC from above showing the SPS, LHC and the four main experiments of the LHC: ATLAS, CMS, LHCb, and ALICE. The standard cartesian coordinate system is shown with its origin at the ATLAS interaction point, the positive x-axis towards the center of the LHC, the positive y-axis pointing upwards, and the positive z-axis pointing along the beamline towards the "A-side"

in terms of the polar angle by

$$\eta = -\ln \tan\left(\frac{\theta}{2}\right). \tag{5.1}$$

where $\eta = 0$ is in the x-y plane and larger values of $|\eta|$ being closer to the beam axis as can be seen in fig. 5.4.

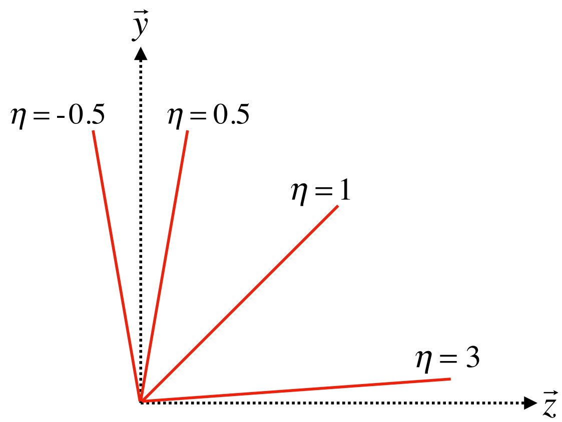

Figure 5.4: Modified from [7] this cartoon represents a selection of pseudorapiditity (η) values overlaid with some cartesian coordinates (dashed black lines). The red lines are drawn for $\eta = \pm 0.5, 1.0, 3.0$

In this analysis the angular separation between objects in the detector is calculated and represented using the geometric quantity

$$\Delta R = \sqrt{(\Delta\eta)^2 + (\Delta\phi)^2} \tag{5.2}$$

5.2 Tracking with the Inner Detector

With its closest component, the Insertable B-Layer (IBL) [8], only 3.3 cm from the interaction point. The Inner Detector (ID), shown in fig. 5.5 [9, 10], faces the incredible challenge of providing precise momentum resolution and identification of both primary and secondary vertex measurements of charged particle tracks all while receiving the highest fluence.

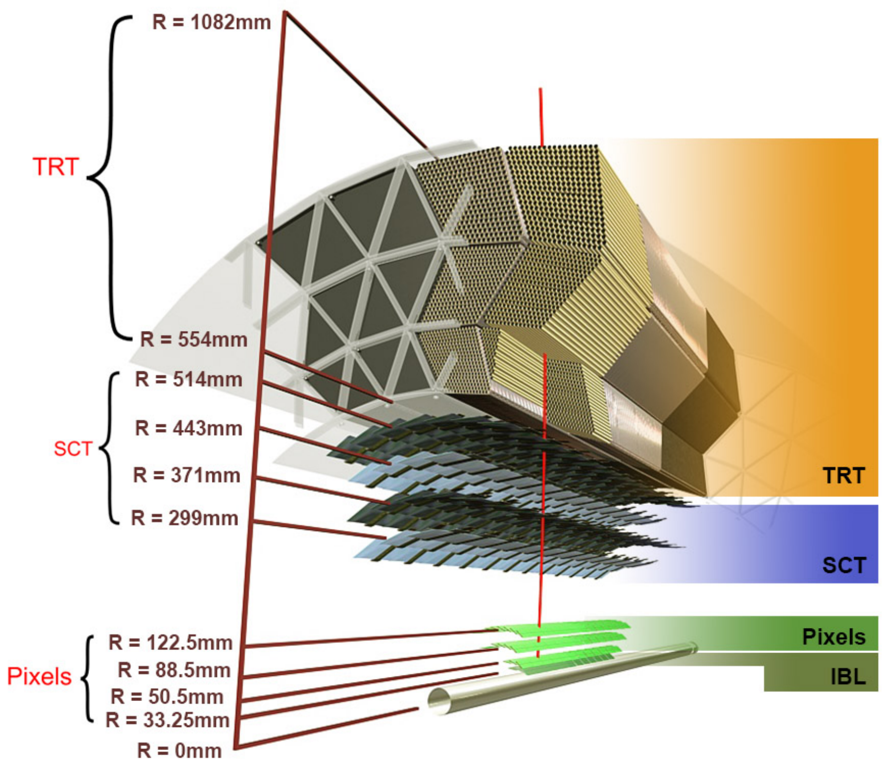

Figure 5.5: [8] Diagram of inner detector

It is designed to be very compact to reduce the probability of a particle decaying inside and to give precision measurements of the particles curvature in the 2T solenoidal magnetic field. This leads to excellent momentum resolution above the nominal p_{T} threshold of 0.5GeV and within the pseudorapidity range of $|\eta| < 2.5$ as shown in fig. 5.6.

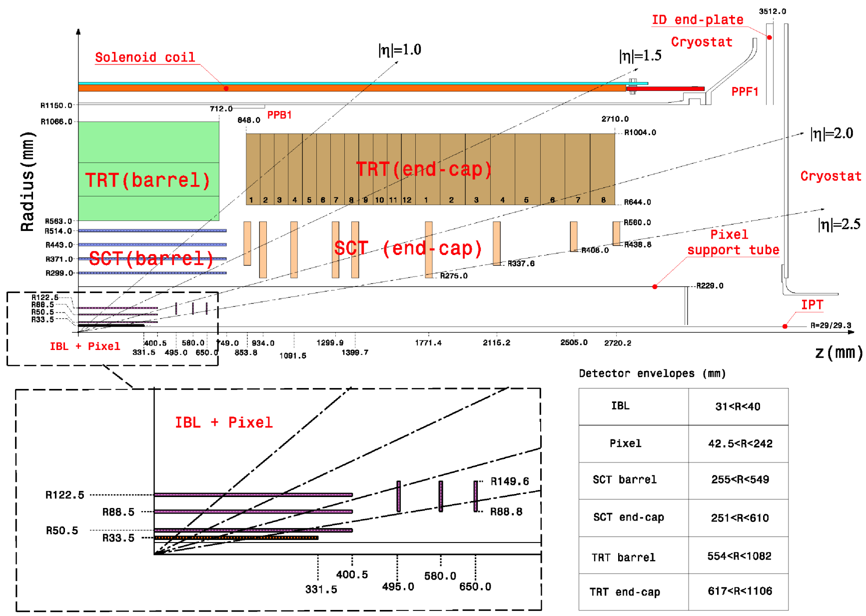

IBL	31<R<40
Pixel	42.5<R<242
SCT barrel	255<R<549
SCT end-cap	251<R<610
TRT barrel	554<R<1082
TRT end-cap	617<R<1106

Figure 5.6: [11] Schematic of the Inner Detector including η lines. Each component shown is cylindrically symmetric leading to a multi-layered detector.

The ID is composed of three different detector technologies for particle trajector reconstruction: Pixel Detector, Semiconductor Tracker (SCT) and the Transition Radiation Tracker (TRT). These will be discussed in the following sections.

5.2.1 Pixel Detector

The ATLAS Pixel Detector [6], the innermost subdetector of the ID, is designed to give the best resolution possible as close as possible to the interaction point. This is accomplished using the 4 barrel layers and 3 disks per endcap as indicated in fig. 5.6. The innermost barrel layer, the IBL, has pixel dimensions of $50\mu\text{m}(\hat{\phi})\times 250\mu\text{m}(\hat{z})\times 200\mu\text{m}(\hat{r})$. For the other layers the dimensions are $50\mu\text{m}(\hat{\phi})\times 400\mu\text{m}(\hat{z})$ for about 90% of the pixels and $50\mu\text{m}(\hat{\phi})\times 600\mu\text{m}(\hat{z})$ for the others, all with a thickness of $250\mu\text{m}(\hat{r})$. This gives a total active area of 1.88m^2 collected through 92.4 million readout channels, more than half of the total number of channels for ATLAS. This detailed charged particle information very close to the interaction point is crucial not only for pattern recognition and track reconstruction, but also for the reconstruction of the primary and secondary verticies intrinsic to the decay of b-hadrons, a critical element of the analysis presented in this thesis.

5.2.2 Semiconductor Tracker

Encompassing the Pixel Detector, the Semiconductor Tracker (SCT) [6] is composed of double-sided silicon microstrip modules. Each side of the 4088 modules is constructed out of two silison strip sensors that are daisy-chained togeather. The result is 768 composite strips each 12.6cm with an inter-strip pitch of 80μm. In the barrel the strips are alligned with the $\hat{z}$ direction, while in the end-caps they are aligned with the $\hat{r}$ direction. In both cases the separation of the strips is constant in $\hat{\phi}$. The two sides are rotated with respect to each other by 40μm to allow for position measurement along the length of the strip. These modules are then used to tile the 4 barrel layers and 9 disks per endcap (18 disks in total) as seen in fig. 5.6. This design is chosen to ensure that each charged track interacts with 8 strip layers (equivalent to four space points). This information is used to further measure the momentum and impact parameter, as well as vertex identification of charged particles.

5.2.3 Transition Radiation Tracker

The Transition Radiation Tracker [6], the outermost subdetector of the ID, provides tracking through the detection of transition radiation from ultra-relativistic charged particles for $\eta < 2.0$ using 350,000 drift tube channels also known as straws. The 4mm diameter straws are filled with a 70% Xe, 27% CO_2, and 3% O_2 gas mixture and a 31μm diameter gold-plated tungsten wire anode at the center for the collection of the ionization signal. In the barrel 73 azimuthally symetric layers of 144cm straws are oriented parallel to the beam pipe with an electrical division in the center of each allowing the two sides to be read out separately. For each endcap the straws are radially oriented in 160 symmetric planes each containing 768 37cm long drift tubes shown in fig. 5.6. In both the barrel and the endcaps polypropylene fibers (barrel) or foils (encaps) function as the transition radiation material which causes the relativistic charged particles to radiate and thus ionize the gas in the straw. The amount of transition radiation produced is proportional to the Lorentz factor meaning that lighter particles (e.g. electrons) will produce more radiation. Thus, by defining a high and low threshold, we can identify tracks belonging to electrons by requiring they register more high-threshold hits. There are typically 36 TRT hits per charged particle track.

5.3 Calorimetry

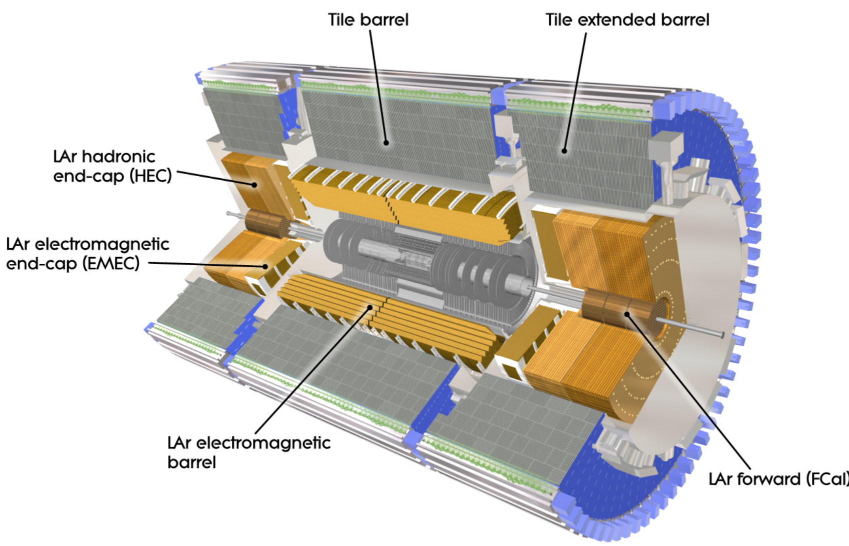

Figure 5.7: [6] A cutaway diagram of ATLAS sampling calorimeters

Once the proton-proton collision remnants have passed through the ID and its surrounding solenoid they enter into the ATLAS calorimeters depicted in fig. 5.7. Sampling calorimeter technologies were choosen for their compact geometry and lower cost point. These are constructed by alternating layers of absorber, a dense material which reduces the incident particles energy, and active material which produces a detectable signal when a particle passes through. This means that the detected signal is only a fraction of the total energy of the particle and thus requires a study of the calorimeter response for calibration purposes [12]. The first system, the Electromagnetic Calorimeter (EMC), is designed to measure the energy of electrons and photons which primarily lose their energy via bremsstrahlung and pair production electromagnetic interactions. Outside of the EMC is the Hadronic Calorimeter (HCal) which is designed to measure the energy of jets of hadrons through their electromagnetic and strong interactions. These detectors cover the entire $|\eta| < 4.9$ range and provide complete containment of both Electromagnetic and Hadronic showers with higher granularity in the EMC for $|\eta| < 2.5$, the region matched to the ID, for precision measurements of electrons and photons. By instrumenting this huge space in $|\eta|$ we can search for events with asymetric energy deposits which imply the existence of a particle we didn't detect represented by missing transverse energy $E_{\mathrm{T}}^{\mathrm{miss}}$.

5.3.1 Electromagnetic Calorimeter

The innermost calorimeter, the Liquid Argon (LAr) Electromagnetic Calorimeter (EMC) [6], uses Lead as the absorber and Liquid Argon as the active material in an "accordion geometry" as seen in fig. 5.8. This geometry was chosen for uniform coverage in $\hat{\phi}$ due to its lack of un-instrumented cracks in the radial direction. The barrel region covers $|\eta| < 1.475$ and an end cap on each side covers $1.375 < |\eta| < 3.2$ each housed in their own cryostat. The barrel is composed of two half barrels with a 4mm gap at $z = 0$ and both end caps are divided into an inner wheel covering $2.5 < |\eta| < 3.2$ and an outer wheel covering $1.375 < |\eta| < 2.5$.

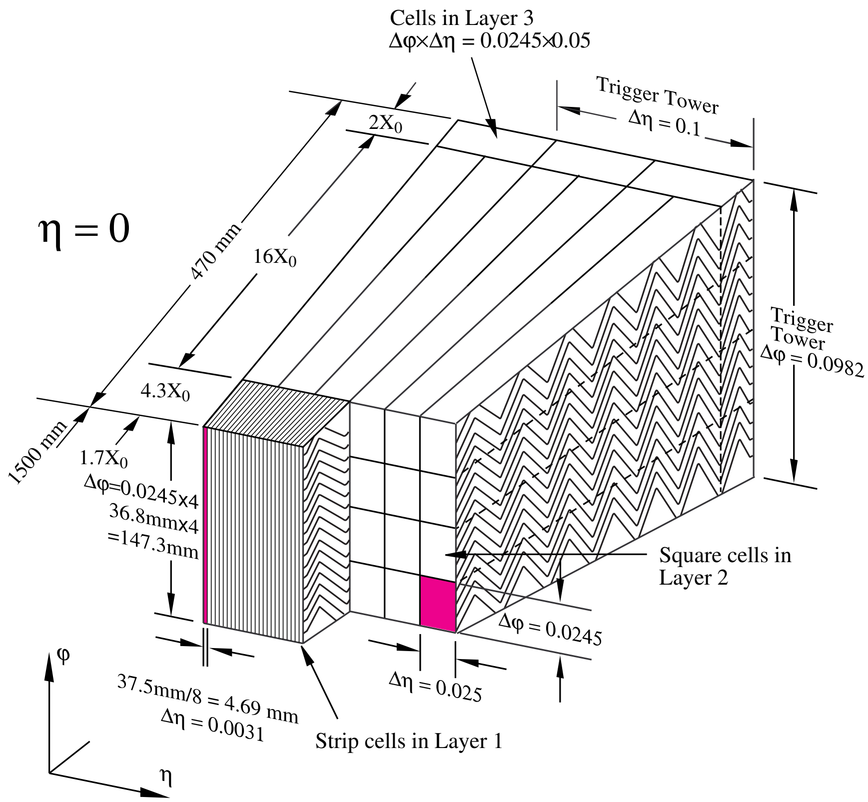

Figure 5.8: [6] Sketch of LAr EMC barrel module where the lead and liquid argon layers are visible in an accordion like geometry. Looking from the foreground to the back there are 3 different types of cells visible.

In the $|\eta| < 2.5$ region the EMC has 3 radial layers for precision physics measurements. Layer 1 consists of strip cells which are finely segmented with $\Delta\eta = 0.0031$ and $\Delta\phi = 0.0245$ allowing for precision position resolution which gives discrimination power between a single γ deposit and the π^0 characteristic $\gamma\gamma$ deposit. Layer 2 , which collects the largest fraction of energy from electromagnetic shower, is segmented with

$\Delta\eta = .025$ and $\Delta\phi = 0.0245$. Layer 3 collects the tail of the electromagnetic shower using a coarser segmentation of $\Delta\eta = .05$ and $\Delta\phi = 0.0245$. Additionally, in the region $|\eta| < 1.8$ a thin pre-sampler , which contains no lead absorber, was placed in front of Layer 1 to allow for energy corrections due to losses upstream of the EMC. Combined the EMC is > 22 radiation lengths (X_0) in the barrel and > 24 X_0 in the end-caps, where a radiation length is the average distance an electron travels in a given material before losing $1/e$ of its original energy E_0 via bremsstrahlung radiation.

5.3.2 Hadronic Calorimeter

Directly outside the EMC envelope is the Hadronic Calorimeter (HCal) system [6] which consists of three sampling calorimeter technologies: the Tile calorimeter, the LAr hadronic end-cap calorimeter (HEC) and the LAr forward calorimeter (FCal). Combined, these three subsystems give measurements of hadronic jet energies in the $0 < |\eta| < 4.9$ range. The tile calorimeter uses steel as the absorber layer and scintillating tiles as the active material and covers the region $|\eta| < 1.7$ with a barrel section flanked by two barrel extensions each divided azimuthally into 64 modules. These scintillator tiles are read out on two sides by wavelength shifting fibers connected to photomultiplier tubes as seen in fig. 5.9. At $\eta = 0$ the total tile calorimeter thickness is 9.7 nuclear interaction lengths (λ), where λ is the average distance a hadron travels before interacting inelastically with a nucleus.

The HEC is composed of two independent wheels per end-cap located just past the

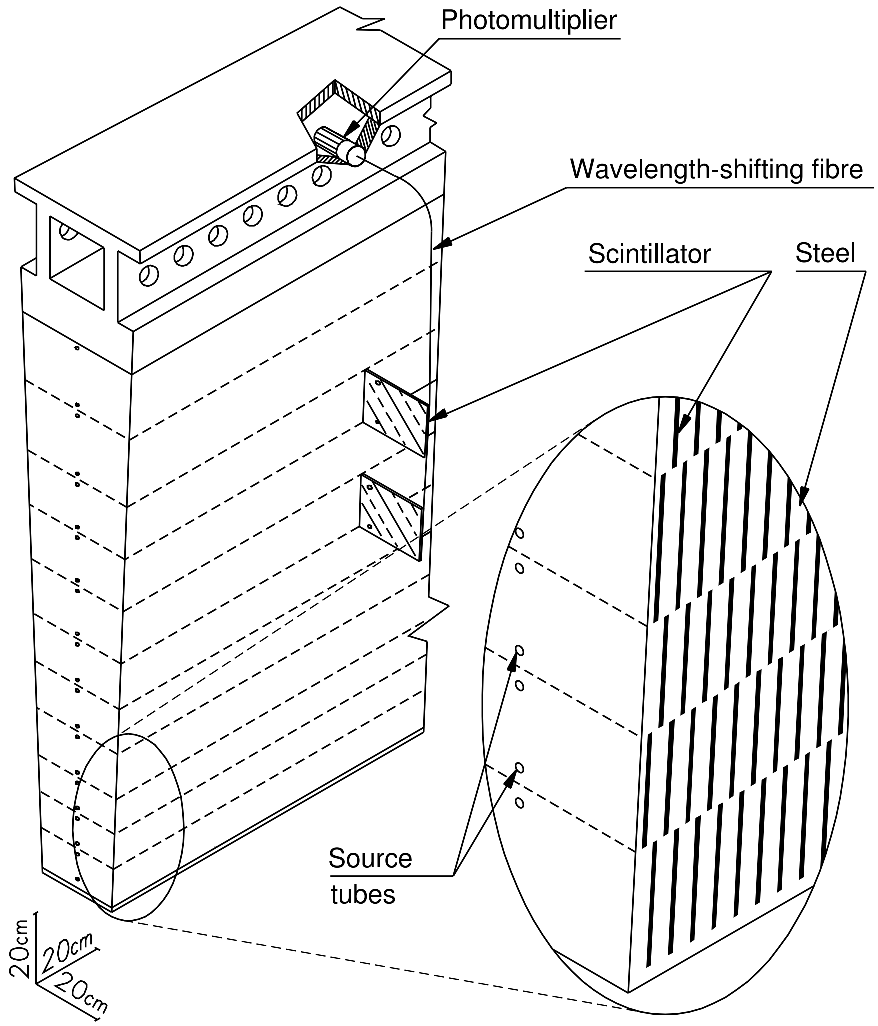

Figure 5.9: [6] Schematic of a tile calorimeter module including a depiction of the connection between the scintillator tile to the photomultiplier via a wavelength-shifting fibre.

EMC end-cap but sharing the same cryostat. This system uses copper as an absorber and liquid argon for the active material and covers the $1.5 < |\eta| < 3.2$ range using 32 wdge-shaped modules per wheel. Finally, the FCal shares the same cryostat as the EMC and HEC end-caps and acts to extend the coverage of the combined calorimeter system to include the $3.1 < |\eta| < 4.9$ range. Each endcap contains 3 modules, the first an electromagnetic module (Copper/Liquid-Argon) which is followed by two hadronic modules which use (Tungsten/Liquid-Argon).

5.4 Muon Spectrometer

The ATLAS Muon Spectrometer (MS) [6], see fig. 5.10, accomplishes tracking of muons in the $|\eta| < 2.7$ region for momentum reconstruction while also triggering on charged particles in the $|\eta| < 2.4$ region. The magnetic field necessary for momentum reconstruction is provided by 3 air-core toroid systems, one barrel toroid covering $|\eta| < 1.4$ and two endcap toroid systems which are inserted into the inner radius of the the barrel toroid to cover the $1.6 < |\eta| < 2.7$. The so called transition region $1.4 < |\eta| < 1.6$ between these two magnet systems is covered by a combination of the barrel and end-cap toroid magnets. Similar to the ID the resolution is inversely proportional to the particle's incident momentum. Any muon with p_{T} lower than 3GeV will never make it to the MS and thus will not be detected.

Precision tracking measurements for momentum reconstruction is accomplished using

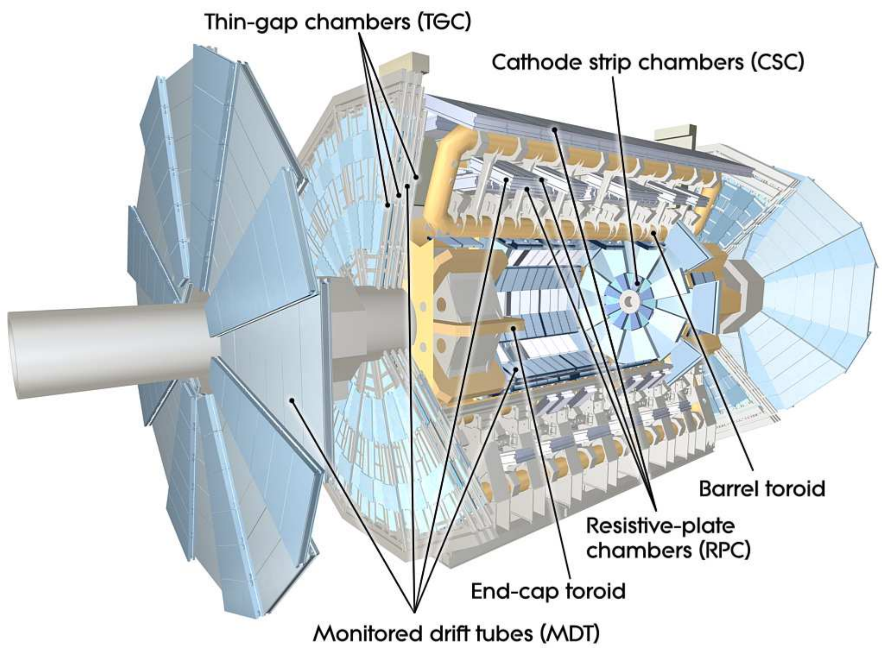

Figure 5.10: [6] A cut-away diagram of the ATLAS muon system and its many sub-detectors.

the Monitored Drift Tube chambers (MDTs) for $|\eta| < 2.0$ and using Cathode-Strip Chambers (CSCs) for $2.0 < |\eta| < 2.7$. The MDT system consists of 1163 drift tube chambers arranged in three to eight layers for varying η. The CSCs are designed to withstand the higher rate and retain good time resolution using multiwire proportional chambers with orthogonal segmented cathode planes.

The MS also gives nanosecond tracking information for triggering on muon tracks. This is accomplished using Resistive Plate Chambers (RPC) in the barrel region $|\eta| < 1.05$ and Thin Gap Chambers (TGC) in the end-cap $1.05 < |\eta| < 2.4$ region. Both chamber systems deliver a triggerable signal with a spread of $15-25$ ns, thus providing the ability to tag individual beam-crossings.

Part III

The HbbISR Analysis

Chapter 6

Data and Simulation Preparation

In order to compare data to theory ATLAS has developed an anlysis chain which runs both real data and simulated samples through the same processing, assuring a final result which is as comprable as possible.

6.1 Data Used

6.2 Monte Carlo Samples

Chapter 7

Physics Object Selection

After the ATHENA Digitization step both data and monte carlo have the same format, representing the three dimentional energy deposits. In order to analyze these deposits they are cleaned, clustered and checked for overlap resulting in physics objects useful for our specific analysis.

7.1 Calorimeter Jets

7.2 Track Jets

7.3 Fat Jets

7.4 B-tagged Jets

7.5 Muons

7.6 Overlap Removal

Chapter 8

Event Selection

Having created our physics objects we begin to make selections of what types of events we want to consider given the goal of our analysis. In our boosted topology this means considering things like momentum, jet collection efficiencies and background rejection.

8.1 Selected Triggers

8.2 Pre-selection Studies

8.3 Signal Selection

8.4 Optimisation

Chapter 9

Background Estimation

The dominant background was QCD. I worked on the ttbar control region. The Vqq and single top backgrounds were estimated from monte carlo.

9.1 Multi-jet QCD estimation

9.2 $t\bar{t}$ control region

9.3 Single top estimation

9.4 Hadronic vector boson channel

Chapter 10

Systematic Uncertanties

10.1 Theoretical Uncertanties

10.2 Experimental Uncertanties

Chapter 11

Statistical Fit

The statistical fit in our analysis was accomplished using a framework developed for Higgs searches.

11.1 Profile Likelihood Function

11.2 Fit Configruation

11.3 Statistical Tests

Chapter 12

Results

12.1 Expectations

12.2 Statistical Analysis Results

12.3 Measurements and Limits

Part IV

Conclusion

Chapter 13

Conclusion

I conclude that this secion is the conclusion

Bibliography

[1] Particle Data Group. "Review of Particle Physics, Chapter 11: Status of Higgs Boson Physics". In: *Phys. Rev. D* 98 (3 2018), p. 030001. DOI: 10.1103/PhysRevD.98.030001. URL: https://link.aps.org/doi/10.1103/PhysRevD.98.030001 (cit. on pp. 22, 24, 27, 29).

[2] L. A. Harland-Lang et al. "Parton distributions in the LHC era: MMHT 2014 PDFs". In: *The European Physical Journal C* 75.5 (May 2015), p. 204. ISSN: 1434-6052. DOI: 10.1140/epjc/s10052-015-3397-6. URL: https://doi.org/10.1140/epjc/s10052-015-3397-6 (cit. on p. 26).

[3] Georges Aad et al. "Measurements of the Higgs boson production and decay rates and constraints on its couplings from a combined ATLAS and CMS analysis of the LHC pp collision data at $\sqrt{s} = 7$ and 8 TeV". In: *JHEP* 08 (2016), p. 045. DOI: 10.1007/JHEP08(2016)045. arXiv: 1606.02266 [hep-ex] (cit. on pp. 29–32).

[4] Lyndon Evans and Philip Bryant. "LHC Machine". In: *JINST* 3 (2008), S08001. DOI: 10.1088/1748-0221/3/08/S08001 (cit. on p. 35).

[5] Chris Llewellyn Smith. “Genesis of the Large Hadron Collider”. In: *Phil. Trans. Roy. Soc. Lond.* A373.2032 (2014), p. 20140037. DOI: 10.1098/rsta.2014.0037 (cit. on p. 35).

[6] ATLAS Collaboration. “The ATLAS Experiment at the CERN Large Hadron Collider”. In: *JINST* 3 (2008), S08003. DOI: 10.1088/1748-0221/3/08/S08003 (cit. on pp. 46, 48, 54–62).

[7] Giordon Holtsberg Stark. “The search for supersymmetry in hadronic final states using boosted object reconstruction”. Presented 26 Apr 2018. May 2018. URL: https://cds.cern.ch/record/2317296 (cit. on pp. 50, 51).

[8] Karolos Potamianos. *The upgraded Pixel detector and the commissioning of the Inner Detector tracking of the ATLAS experiment for Run-2 at the Large Hadron Collider*. Tech. rep. ATL-PHYS-PROC-2016-104. 15 pages, EPS-HEP 2015 Proceedings. Geneva: CERN, Aug. 2016. URL: https://cds.cern.ch/record/2209070 (cit. on p. 52).

[9] *ATLAS inner detector: Technical Design Report, 1*. Technical Design Report ATLAS. Geneva: CERN, 1997. URL: http://cds.cern.ch/record/331063 (cit. on p. 52).

[10] S Haywood et al. *ATLAS inner detector: Technical Design Report, 2*. Technical Design Report ATLAS. Geneva: CERN, 1997. URL: https://cds.cern.ch/record/331064 (cit. on p. 52).

[11] B. Abbott et al. “Production and integration of the ATLAS Insertable B-Layer”. In: *JINST* 13 (2018), T05008. DOI: `10.1088/1748-0221/13/05/T05008`. arXiv: `1803.00844 [physics.ins-det]` (cit. on p. 53).

[12] Christian Wolfgang Fabjan and F Gianotti. “Calorimetry for Particle Physics”. In: *Rev. Mod. Phys.* 75.CERN-EP-2003-075 (Oct. 2003), 1243–1286. 96 p. DOI: `10.1103/RevModPhys.75.1243`. URL: `https://cds.cern.ch/record/692252` (cit. on p. 57).

Appendix A

Hadronic Vqq Sherpa Studies

Ancillary material should be put in appendices, which appear after the bibliography.